3D printing of bio-inspired, multi-material structures to enhance stiffness and toughness

A thesis

submitted in fulfilment

of the requirements for the degree

of

Master of Engineering

in

Materials and Process Engineering

at

The University of Waikato

by

Xinhan Zhang

THE UNIVERSITY OF
WAIKATO
Te Whare Wānanga o Waikato

2021

Abstract

In nature, many biological, multi-materials have complex microstructures and excellent mechanical properties. One shellfish material called nacre has received much attention due to its unique interlocking structure of alternating calcium carbonate tablet and soft organic matter filler. It has microstructure features such as waviness which provide high strength and toughness properties. As a popular topic in the study of bio-inspired structure, it is of great significance to study the ordered microstructure and toughening mechanism of nacre.

3D printing allows for the easy manufacture of complex structures. In this project, inspired by the high strength and toughness of natural nacre, 3D printing technology was used to prepare nacre-like, multi-material structure. Tensile tests, cyclic tensile test and fracture toughness tests were carried out to investigate the relationship between multi-material structure geometry and tensile properties, fracture modes and toughness behaviour.

In the experimental part of this thesis, specimens of the tablet-filler with different dovetail angles made by polylactic acid (PLA) and thermoplastic polyurethane (TPU) inspired by the microstructure of nacre structure were prepared through Fused filament fabrication (FFF)/ Fused Deposition Modelling (FDM) type of 3D printing technology. The multi-material dovetail PLA & TPU specimens exhibited multi-stage deformation under tensile testing. By comparing the tensile performance of structure made by dovetail PLA & PLA material as well as unidirectional pure PLA specimen, it was confirmed that the incorporation of soft TPU filler gave the opportunity for tablet sliding, resulting in a complex multi-stage deformation mechanism of the structures.

Two modes of failure mechanisms, tablet pull-out and tablet break, were observed for the multi-material PLA & TPU structure under tensile testing. The combination of tablet break and pull-out modes can lead to higher strength and modulus than tablet

pull-out. In the tablet pull-out mode, transverse expansion was observed in the larger angle dovetail structure, and the occurrence of negative Poisson's ratio effect was determined by calculation. In addition, there is a distinct plateau stage in the tensile curve of multi-material PLA & TPU structure, through cyclic tensile tests identified the plateau as a yield point, generated by short interface between tablets and filler broken. The cyclic tensile tests also determined that the main deformation resistance of the PLA & TPU structure was provied by the long interface broken between tablets and filler, also the interlocking and shearing between the dovetail angle tablets.

Multi-material PLA & TPU structures with larger dovetail angles produced greater plastic deformation and absorbed more energy during tensile testing. Multi-material PLA & TPU with 5˚ dovetail showed the highest ultimate tensile strength 11.46 MPa and Young's modulus of 495.96 MPa, but 9˚ dovetail performed poorly with 6.51 MPa and 395.48 MPa, respectively. The value even below than 1˚ dovetail (ultimate tensile strength of 9.82 MPa, modulus of 453.38 MPa). The ultimate tensile strength and Young's modulus of the multi-material PLA & TPU structure are not as high as those of unidirectional pure PLA and dovetail PLA & PLA specimen, but energy absorption performance is improved by soft TPU filler and dovetail angles. In fracture experiments, crack extension behaviour was observed in fracture toughness specimens.

In summary, the mechanical properties of the nacre-like, multi-material structure were investigated by tensile behavior, fracture mode and energy absorption analysis in this paper. It is demonstrated that the combination of stiff tablet material and soft filler material can effectively improve the toughness of the structure. The tensile strength of the multi-material structure can be improved by increasing the dovetail angle of the tablet. However, it has not been observed that increasing the dovetail angle can significantly increase stiffness. It is confirmed that the optimized design of the 3D printed, bio-inspired, multi-material structure can change the mechanical behavior of

the structure and improve its mechanical properties, can provide new ideas for the development of composite materials with excellent mechanical properties.

Acknowledgements

This research work was completed under the supervision of Dr. John McDonald-Wharry. His strict supervision and meticulous work helped me improve my research writing, increased my academic ability and inspired my research ideas. I sincerely thank Dr. John McDonald-Wharry for helping me with project preparation, experimental design, and analysis of conclusions. The skills I learned from Dr. John McDonald-Wharry will have a profound impact on my future study and work, which is my precious and lucky harvest.

I need to thank the members of the research group, Xutao (Brian) Sun, Christian Gauss and technician officer Duncan Barnard, who helped me a lot with the data calculation and operation of experimental equipment and also shared their research experience, especially at the start of my project.

A big thanks go to my friends Yaqi Chang, Jingnan Ma and Yuning Zhao, for accompanying me in the master life, I got so much from yours and without your encouragement, I can’t finish the master study.

Sincere thanks to my parents, for their silent dedication and full support. Although we are separated from each other in different countries, they did not neglect their concern for my life and study. Their financial support ensured my master study could be finished without any hindrances, and also their understanding encourages me to follow the difficult life of studying abroad.

My thanks to the many others who I could not specify directly.

Table of Contents

List of Figures

List of Tables

List of Abbreviations and Nomenclature

3D printing technologies

Abbreviation	Full name
FFF	Fused filament fabrication
FDM	Fused deposition modelling
SLS	Selective laser sintering
SLM	Selective laser melting

3D printing Filament

Abbreviation	Full name
ABS	Acrylonitrile butadiene styrene
PLA	Polylactic acid
TPU	Thermoplastic polyurethane

Multi-material specimen names

Specimen Abbreviation	Details
PLA & PLA	PLA filament used as tablets material, PLA filament used as filler material
PLA & TPU	PLA filament used as tablets material, TPU filament used as filler material
Pure PLA	Unidirectional tensile specimens made by pure PLA

Chapter 1

Introduction

At present, to satisfy the needs of high technology, researchers have invented composite materials based on the improvement and combination of different materials, which has far exceeded the performance of traditional single materials and is developing towards direction of higher stiffness, higher strength, and other ultra-high performance. Bio-inspired materials is an important branch of materials science and provided much inspiration for the study of new composite materials. After a long period of evolution, organisms have achieved excellent overall mechanical properties between their structures and components.

Some shellfish shells exhibit great combination of high strength and toughness, which is almost impossible to achieve with human-made materials [1]. Their mechanical properties result from a mixture of multi-scale toughening mechanisms, with the nacre consisting of 95% aragonite lamellar made of calcium carbonate (or tablets) and 5% of organic protein layers (referred to as filler) and arranged in a parallel interlocking way [2]. This structure allows it to exhibit a higher stiffness and strength and a toughness that can reach thousands of times that of its constituent materials [3]. It is generally accepted that the relative sliding between the layers of aragonite tablets is the basic deformation mechanism of nacre and the basis for their high strength and toughness [2, 4]. The waviness of the tablets in the nacre layer helps to lock in and promote large-scale strain hardening. In addition, microstructures such as mineral bridges [5] and surface roughness [2] are present in the internal aragonite lamellae of nacre, all of which have a significant influence on the mechanical properties of nacre-like materials. Typical deformation and failure modes such as filler viscoelastic energy dissipation and tablet pull-out accompany the sliding process of the tablets, while tablets fracture can significantly increase the strength of nacre-like composites [2].

Complex biological microstructures in synthetic composites can be easily constructed using advanced multi-material 3D printing techniques. Here, in this project, multi-material 3D printing was used to prepare tensile specimens and toughness specimens of multi-material structures with different dovetail angles based on the natural nacre structure. The tensile response, fracture behavior and mechanical properties of the bio-inspired, multi-material structure at different stages will be observed and analyzed. It is of great scientific significance and engineering application to reveal the mechanism of toughness of nacre-like materials and to develop new methods to construct human-made, advanced materials that mimic resemble the structure and function of natural materials.

1.1 Research objectives

The purpose of this thesis is to design and construct a 3D printing, multi-material structure with high strength, stiffness and toughness by combining multiple materials with different properties.

This project had the following aims:

- Fabricate the multi-material structures through multi-material FFF/FDM 3D printing.
- Investigate the effect of stiff and soft material composition on the tensile performance of the multi-material structures.
- Investigate the effect of different dovetail angles on the tensile properties of multi-material structures.
- Observe the fracture behavior of the multi-material structure to confirm whether there is a negative Poisson's ratio effect.

Chapter 2

Literature review

3D printing, also known as additive manufacturing (AM), is a rapid prototyping technology that uses 3D modeling computer software to rapidly manufacture solid parts, models or components [6]. It contributes three-dimensional construction through computer control and usually printing by adding materials layer-by-layer. This combination allows the fine and detailed structure to be printed without assembly. Since the first equipment originally used for rapid prototyping (RP) was launched in 1988, more than ten different forming technologies, such as fused deposition modelling (FFF)/ fused filament fabrication (FDM) [7], selective laser sintering (SLS) [8] and inkjet printing [9], have emerged since the development of 3D printing technology.

The existing 3D printing technology has realized efficient and low-cost manufacturing of complex 3D structures on macro-scale [10]. Compared with traditional processing technology, 3D printing technology has obvious advantages: 3D printing can greatly reduce the cost of product innovation and produce complex lattice structures at a lower cost [11]. It has the high precision to form a complex 3D structure that can simplify the production process and reduce material waste. 3D printing also performs well at multiple scales, enabling macro-scale structural printing and micro-nano-scale 3D printing, respectively, and realizes the functional printing of living bodies, like the parts of the human body [12, 13].

There are also many limitations to 3D printing, the most significant being the limitations of materials. The filament materials used for 3D printers are limited, only some plastics, metals or ceramics can be printed [14], and most of them cannot be recycled. The printing machine is another issue, which limits the size of the printing parts. Also, the printing speed is not efficient [15], and the strength of the printed part

is not guaranteed. There are also copyright issues, the popularity of 3D printing makes it increasingly possible to create counterfeit products [16].

Single-material 3D printing has gradually become difficult to meet the performance requirements of products in industrial production. The developing 3D printing now can print different materials with different properties into the same structure, realize multi-material and multi-scale printing of composite materials and functional gradient materials, and achieve integrated design and manufacturing of materials, structures and functional components [17]. Multi-material 3D printing represents the future development direction of additive manufacturing technology, with great potential and broad application prospects [18-20].

2.1 Additive manufacturing technologies

Depending on the form of the input material, 3D printing can be divided into three types: solid, liquid and powder [21]. The most common of the solid types is the Fused Filament Fabrication (FFF)/ Fused deposition modelling (FDM) printing, the liquid types are based on the same principles as traditional 2D printers, such as Inkjet printing. The powder type printing includes Selective laser sintering (SLS) and Selective laser melting (SLM).

2.1.1 Fused filament fabrication (FFF)/ Fused deposition modelling (FDM)

Fused filament fabrication (FFF), also known as Fused deposition modelling (FDM) (a commercial copyright term), is one of the most widely used additive manufacturing processes for manufacturing plastic prototypes and functional components [7]. The working principle of FDM is to heat and melt filamentous thermoplastic materials through a nozzle. Under computer control, the nozzle moves to the specified position according to the G-code of the 3D model. The liquid material in the molten state is extruded and the structure is constructed layer-by-layer. After extruding the material, it is deposited on the solidified material of the previous layer, and the final product is

formed by stacking the material layer-by-layer, which also leads to anisotropic mechanical properties [22]. It is important to study the mechanical properties of FDM printed structures when studying different types of material filament and pattern features.

FDM is a complex process. There are a large number of parameters that affect the mechanical properties of the product, such as printing direction, layer thickness [23], printing temperature [24] and feed rate, which have an important impact on the quality and performance of FDM printed parts. Chacón et al. analysed the influence of printing direction, thickness and feed rate on the mechanical properties of low-cost PLA 3D printing products. The results show that 3D printing products have anisotropic behaviour, the mechanical properties of vertical direction are the lowest, and the edge and plane direction has the highest strength and hardness [25]. In addition, the mechanical properties of the printed parts are enhanced with the increase of the layer thickness as the feed rate increases. Giovanni et al. analysed PLA 3D printed parts with filling patterns of linear filling and honeycomb filling by fracture toughness testing, the specimen results showed the filling density has more influence on the fracture life [26].

2.1.1.1 Materials used as FDM/FFF filament:

As a hot-melting process, the thermoplastic filament should be melted before the deposition process. Generally, the applicable materials have suitable thermal properties, such as Acrylonitrile butadiene styrene (ABS), Polylactic acid (PLA) and Thermoplastic polyurethane (TPU). The filament material should also have the required bending, compressive and tensile strengths, as well as sufficient bonding between the layers during printing [27].

ABS (Acrylonitrile butadiene styrene)

ABS is a widely used thermoplastic material in FDM, which has sufficient melt fluidity, ideal stiffness, and strength [28]. The tensile, compressive and bending strengths of

FDM parts made of ABS are lower than injection moulded parts [19]. This material has the property of shrinking while cooling and will partially peel off from the printing plate and may peel off entire layers if printing tall objects, so heating the printing bed is necessary.

PLA (Polylactic acid)

Polylactic acid (PLA) is another commonly used thermoplastic material in FDM. It is a biodegradable biopolymer, usually made from maize starch or sugar cane via fermentation[29], which tends to break down naturally in about three to six months [30]. The elongation at break of PLA is lower than ABS, but the strength is higher [31]. Polylactic acid is more promising because of its high rigidity and high mechanical strength [32].

Due to good biocompatibility, processability and degradability, PLA and its composites are considered to be the most promising new biopolymer materials [33, 34]. 3D printing products with PLA materials have been widely used in biomedical fields including medical models, bone tissue repair scaffolds and drug delivery systems [35]. Tao et al. optimized the prosthetic model, which could be printed directly from a 3D printer, simplifying the manufacturing process. The PLA prosthesis made by the FDM method was 62% lighter than those made by traditional methods, which is helpful to improve the quality of life for patients [36].

TPU (Thermoplastic polyurethane)

Thermoplastic polyurethane elastomer (TPU) is an elastomer which can be melted by heating or dissolved in solvent. It has great properties, including fine abrasion resistance, high elongation and some types also have good biocompatibility [37]. It has good processing performance and is widely used in national defence, medical, food and other industries. However, there are limitations to its application due to its poor shape forming and low mechanical strength [38].

Composites

The energy absorption properties of composites has been proved that can be effectively improved by adding fibres into thermoplastic materials [39]. Carbon fibre is a fibre composed of carbon, with a diameter of about 5 to 10 mm [40]. It has the characteristics of light weight, good electric conduction, heat conduction and corrosion resistance [41]. Carbon fibre is mainly compounded to reinforce materials such as resin, metal, ceramic and carbon to make advanced composite materials. Nakagawa et al. embedded continuous carbon fibre filaments in middle of the mixtures with ASB and short-cut carbon fibre which printed by the FDM method to create carbon fibre reinforced plastics, the strength of carbon fibre composite can be much stronger than a single plastic [42]. Tekinalp et al. prepared composite samples with high fibre isotropy by adding short-cut carbon fibres to ABS by the FDM method. Compared with traditional injection moulding samples, the tensile strength of 3D printed samples with 40% fibre content increased by 115% , reaching 65MPa. The microstructure of the internal pores of 3D printed composites shows comparable tensile strength and modulus [43].

Glass fibre is an inorganic, non-metallic material with excellent performance. It has high tensile strength, high elastic modulus and good impact energy absorption, the diameter of a monofilament ranges from 3 to 20 microns [44]. Glass fibre is commonly used as composite materials, electrical insulation materials, insulation materials and circuit boards, etc [45]. In contrast to carbon fibre, glass fibre can undergo more elongation before it breaks [46]. Li et al. blended cellulose and glass fibres with PLA to make a reinforced PLA filament that can be used for FDM printing. The impact strength of this polymer filament was 34-60% higher than that of pure PLA filament and the tensile strength was 43-52% higher than that of pure PLA filament [47].

Natural materials can likewise be applied to 3D printing. Guo et al. investigated the toughening mechanism of poplar wood powder-PLA composites printed by the FDM

method. TPU, polycaprolactone (PCL) and polyethylene-co-octene (POE) were added as toughening agents to the wood powder-PLA composites, respectively. The addition of TPU increased the impact strength of the composites by 51.31% and improved the composite viscosity and modulus of the composites [48].

2.1.2 Selective laser sintering (SLS) and Selective laser melting (SLM)

Selective laser sintering (SLS) is a powder-based technology. It uses the laser as the power source to sinter powder materials such as ceramic powder, metal powder and polymer powder. The laser is automatically aligned to the space points defined by the three-dimensional model, and the materials are bonded together to form a solid structure [18]. The Selective laser melting (SLM) process allows powder materials to be completely melted into solid three-dimensional parts, allowing fully functional parts to be manufactured directly from metal without the use of any intermediate binders or any additional processing steps after the laser melting operation [8].

Laser sintering may change the properties of the material. Researchers have found that the temperature field of laser sintering is inhomogeneous and this temperature evolution has a significant impact on the density, sizes, mechanical properties and microstructure of the final 3D printed part [49]. Contuzzi et al. suggest that this will lead to thermal deformation of the printed part, making it impossible to proceed to the next assembly step [50].

2.1.3 Inkjet printing

Inkjet printers work by using a piezoelectric ceramic or heater at the nozzle [9], which creates a transient boost of pressure at the nozzle, squeezing the ink out of the nozzle and creating the structure. It has the ability to create microfluidic structures and is currently gaining interest from the bioscience community [51]. Microfluidic structures are used in chips to study or control the smallest amount of fluid in the nanolitre range, typically in the format of 26 mm* 76 mm [35]. Walczak et al. proposed a microfluidic

structure for spectrophotometric analysis of beverages, which provides a proof of concept for the application of inkjet 3D printing in microfluidic structure manufacturing [51].

Inkjet printers enable 3D bio-printing by replacing the ink with a bio-ink of similar viscosity, which in cellular bioprinting also ensures cell viability. The combination of 3D printing technology and medicine can solve many of the challenges faced by traditional medicine, such as the lack of transplantable organs for transplant organ rejection. 3D printing technology can realize the 1:1 reproduction of the patient's amputation part and customize a perfect fit prosthesis for amputee patients [52]. 3D printing is also expected to solve the problem of organ transplantation.

2.1.4 Droplet jet lighting curing technology

Droplet jet lighting technology involves spraying photosensitive materials from a porous nozzle and then curing this material by ultraviolet (UV) light using a light source located on the print head plate, which immediately reacts and cures the liquid resin, resulting in a 3D model [53]. When spraying the material, material properties such as print colour and strength or elasticity can be highly controlled [9].

Droplet jet lighting curing technology has been widely used for rapid prototyping of multi-material structures. Currently, the main commercial printers are Connex series printer from 'Stratasys' and Projet series printer from '3D Systems'. Connex500 is a 3D printer that enables large size, high precision and multi-material forming [54]. The printer has print unit with eight print nozzles, each containing 96 nozzles with a diameter of 50 microns [55].

2.1.5 Multi-material printing

Multi-material additive manufacturing techniques can improve the performance of 3D printed parts by adding complexity and functionality [56]. Multi-material does not

mean pre-mixing different kinds of materials, but rather using different materials to create different printed parts in one printing process, which requires different materials to be physically transferred to set spatial locations in three-dimension during the 3D printing process [57]. In the FDM process, the multiple extruders can be installed on the 3D printer or a single extruder with an automatic material switching program [58]. This approach allows different materials to be printed in a single print process, can print combinations of materials with different properties, and can create arbitrary composite structures.

Multi-material printing has great potential for applications in the traditional manufacturing industry and in medical. Multi-material printing allows the fabrication of embedded components as well as the printing of 3D circuits, and a system has been developed by Malone et al. to manufacture and print conductive circuits on components by FDM type 3D printing technology [59]. Khalil et al. have designed a multi-nozzle bio-coating system that can extrude biopolymer solutions and live cells for the free construction of 3D tissue scaffolds [60].

Micro-scale FDM double printing has also proved applicable, with Okwuosa et al. printing 0.52mm tablets onto capsule molds for pharmaceuticals [61]. Multi-material printing technology still has shortcomings, such as printing defects in multi-materials and imperfect combinations between printed materials, which will lead to increased costs and inefficiencies in actual manufacturing [62].

2.2 Mechanical testing methods and properties

2.2.1 Tensile test

Tensile testing is a basic materials science and engineering test in which a tensile force is applied to a material and the response of the specimen to the stress is measured. It determines a range of strengths and properties of the material.

The results of the tensile test can draw the stress-strain curve of the material, and the stress and strain can be determined by gradually applying load to the specimen and measuring the deformation. These curves reveal many properties of materials, such as Young's modulus, yield strength and ultimate tensile strength. The shape of the curve reflects the brittle, plastic, yield, fracture and other deformation processes of materials under external force. The process is generally divided into three stages: linear elastic, strain hardening and necking. Figure 2.1 illustrates the curvilinear properties of polymer material with different characteristics when stretched.

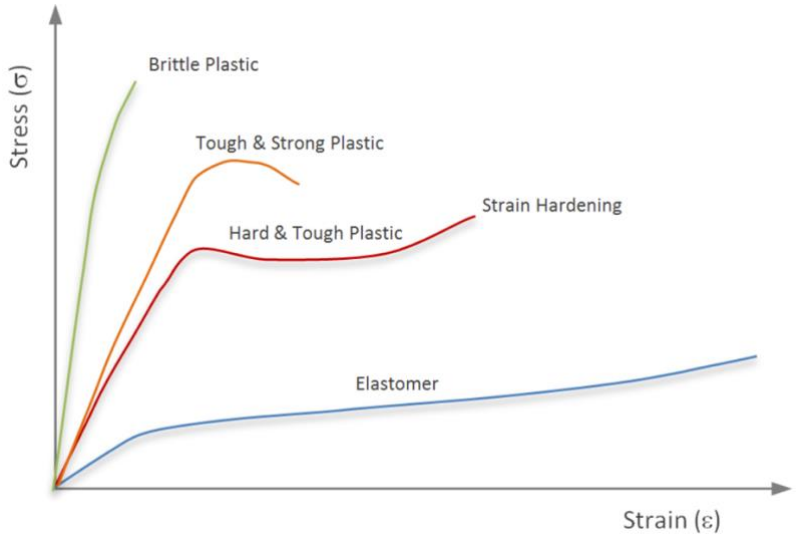

Figure 2.1. Typical stress-strain curve of polymer [63].

Using FDM, Lin et al. printed ABS specimens in the shape of dog bones, depending on the orientation and different fibre diameters, and then subjected them to material tensile tests. The mechanical properties were found to be significantly anisotropic. It has the characteristics of elastic-plastic in the fibre direction and elastic- brittle in the vertical fibre direction [20]. The larger the fibre diameter in the vertical fibre direction, the greater the failure strain. Geng et al. prepared a bio-based polymer by 3D printing, which yielded a tensile strength of 42.7 MPa and an elongation at break of 515% by tensile testing, far exceeding the most commonly used bio-based 3D printed polymers [64].

2.2.2 Impact test

An impact test is a kind of experiment to study the dynamic resistance to impact force of materials. It can determine the energy absorbed by materials in the process of fracture and test the toughness of materials. Different from the static load, the high loading speed will make the stress in the material increase rapidly, and the deformation speed will affect the mechanical properties, so the material shows another different response to the dynamic load [65]. Materials with ductile properties under static load tend to show brittleness under impact load. In addition, some structural characteristics that may affect mechanical properties (such as internal defects of materials) can be found, which is not easy to be found under the static load [9], so impact test is necessary when studying the properties of materials.

There are two types of impact test, the Charpy V-notch test and the Izod impact test. In the impact test, the test apparatus consists of a pendulum of known mass and length which is dropped from a known height to impact a notched material specimen [66]. The energy absorbed by the sample is calculated based on the height the arm swings to after impacting the sample. The difference between Izod impact test and Charpy impact test is that the sample is kept in the cantilever configuration and in the vertical position, while the sample of Charpy impact test is placed horizontally.

Flores-Johnson et al. investigated an impact resistant material inspired by nacre layer structure. The mechanical response and ballistic properties of this layer structure were investigated by impact tests. The experiment simulated the impact of a 10 mm steel spherical projectile against aluminium alloy nacre-like laminates with thicknesses of 5.4 mm, 7.5 mm and 9.6 mm at initial impact velocities of 400-900 m/s. The 5.4mm thick sample at high impact velocities showed great mechanical properties, with the layered structure favouring local energy absorption and more global energy absorption [67]. This is due to the larger plastic deformation area resulting from the tablet arrangement, which is discussed in Section 2.3.2 Nacre shells.

2.2.3 Fracture toughness testing

The ability of a structure to retain its strength in the presence of cracks or defects is one of the fundamental requirements for the design of composite materials [68], and defects can lead to catastrophic failure and a significant reduction in mechanical properties. Fracture toughness describes the ability of a material containing a crack to resist fracture. Fracture mode can be divided into three types based on the stresses at the tip of the decomposed crack, opening mode I for stresses orthogonal to the local plane of the crack surface, shear mode II for stresses parallel to the crack surface but orthogonal to the leading edge of the crack, and anti-plane shear mode III for stresses parallel to the crack surface and the leading edge of the crack [69]. The results are expressed in terms of toughness parameters such as plane strain fracture toughness (K_{IC}), or strain energy release rate (G). The plane strain fracture toughness is defined as the toughness parameter indicative of the resistance of a material to fracture, the strain energy is the toughness parameter based on energy release rate required to fracture [70].

2.2.4 Cyclic loading test

Cyclic loading is the application of repeated or fluctuating stresses, strains, or stress intensities to locations on structural components [71]. The degradation that may occur at the location is referred to as fatigue degradation. Fatigue refers to the process in which a material gradually produces permanent and cumulative damage under the action of cyclic stress or cyclic strain, and cracks or sudden complete fracture occurs after a certain number of cycles [72]. Cyclic loading tests are generally divided into cyclic tensile tests and cyclic compression tests, in which micro cracks will start to sprout at the stress concentration, such as voids, persistent slip bands, composite interfaces or grain boundaries in metals [73]. The nominal maximum stress value causing such damage may be much less than the strength of the material and is usually referred to as ultimate tensile strength or yield strength.

The test rate for cyclic testing is divided into high cyclic and low cyclic loading, with the number of cycles generally determined according to the actual use scenario of the structure.

2.3 Bio-inspired Structures

In nature, many biological structures have complex microstructures and excellent mechanical properties. In the quest to develop high engineering performance materials, many studies inspired by biology are prevalent in different research areas [2, 55, 74-76]. Bio-inspired materials are structuring properties and functions can be further enhanced by the study of biological structures, which are mimicked beyond natural structures [77]. 3D printing technology can help researchers to build simplified structural models of complex biological systems, thus making it easier to study their mechanisms, which greatly supports the study of bio-inspired structures.

2.3.1 Fish dermal armour and 3D printing

People have been able to imitate nature since ancient times. Boats, rudders and oars were invented in the shape of fish and their tails and fins. The underwater parts of torpedoes, submarines and boats can be designed to mimic the shape and skin structure of dolphins, reducing drag by 20-50% [78]. The structure of natural fish skin is divided into a variety of scales, they are usually hard and arranged in an interlocking or buried fashion that can perform a variety of functions such as flexible protection, improved hydrodynamics and body support [76]. Fish skin armour is hard and arranged in an interlocking or buried fashion to minimize resistance to water. Deep-sea sharks can travel at speeds of up to 70km/h [79] and when the skin of sharks is viewed through a microscope it is found that the scales are fan-shaped and have small grooves, as shown in Figure 2.2 (a) (b). In one study, 800 model scales were assembled at different angles to form a single surface, and the results of tests showed frictional losses of up to 10% less than on smooth surfaces [80]. This indicates bio-inspired structures could have benefits in improving the structural performance in practice.

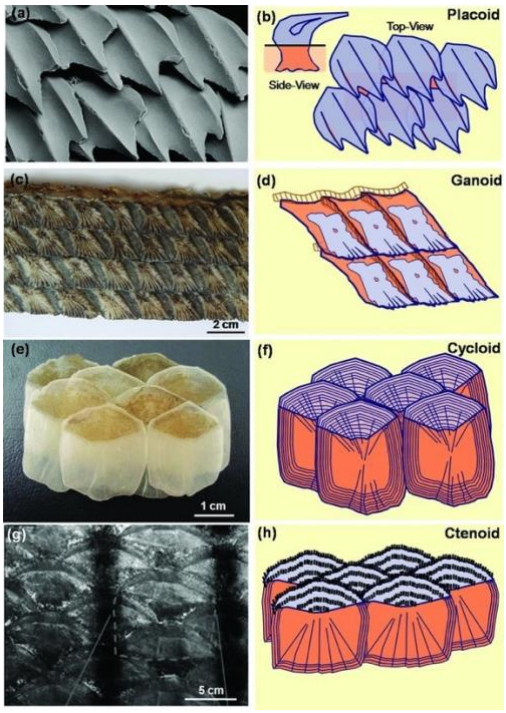

Figure 2.2. Four types of fish overlaps and scales [81]. Reprinted with permission from Advanced Materials

The good mechanical properties of fish skin were shown to come from the arrangement of the individual fish scales. The 3D printing model of overlapping fish scales was established, as shown in Figure 2.3, and plane strain compression [82], three-point bending [83] and compression were performed respectively. Experiments have shown that bending and frictional sliding and shear deformation control the overall mechanical behaviour of the overlapping armour, which is consistent with the behaviour of the fish scale structure predicted by the mechanical model [84].

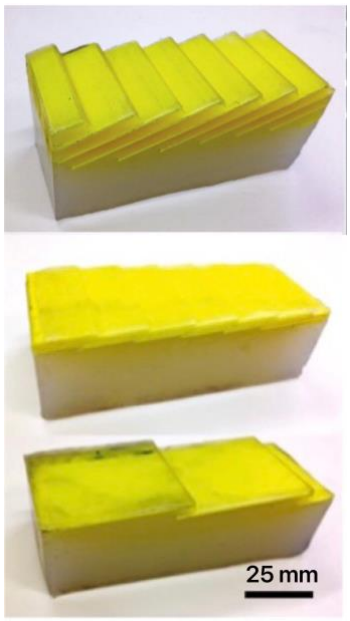

Figure 2.3. 3D printing models with different overlapping sizes [82]. Reprinted with permission from Elsevier.

Mechanical properties can be increased by interlocking simple geometries. The skin of the boxfish consists of a highly mineralized plate with a high degree of mineralisation and a pliable collagen matrix, the superficial plate being predominantly hexagonal with non-mineralised collagen fibres beneath, arranged in layers of thickness through a stepped stratum [85]. At the interface between the scales, the mineralised plates form a serrated structure with collagen fibres beneath them bridging the gap between adjacent scales, as shown in Figure 2.4.

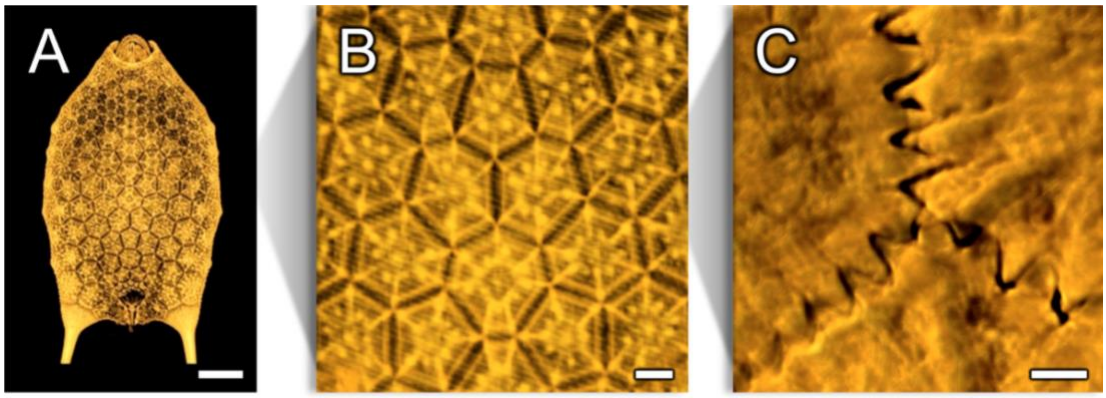

Figure 2.4. (A) Ventral surface of the boxfish's shell in 5mm. (B) Scale arrangement in 1 mm. (C) Serrated suture between adjacent scales in 50µm [85]. Reprinted with permission from Elsevier.

Small-scale boxfish skin samples with 0.7mm long and 2.4mm width were fabricated by Yang et al. based on the serrated interlocking structure. In tensile and compressive tests, the serrated interlocking greatly improved the strength and stiffness property, being more than twice as strong as the non-serrated armour. The serrated boundary lines remained relatively intact, while most failures occurred within the collagen fibres and the individual scales retained their integrity. The organic material between the serrated scales not only increases the surface area contact between the plates, but also acts as a locking mechanism to prevent shearing and sliding between the scales [85].

Lin et al. constructed the boxfish' skin-like samples using an Objet Connex500 3D multi-material printer, using an acrylic-based photopolymer called Vero White for the stiff scales and Tango Plus is rubber-like compliant material as the soft organic material between the scales. The scale boundaries for the model were that they were anti-trapezoidal, rectangular, trapezoidal and triangular as shown in Figure 2.5. Where β indicates the suture angle measured relative to the vertical axis of the anti-trapezoid. The influence of soft Tango Plus between scale boundaries on structural properties is also studied [86].

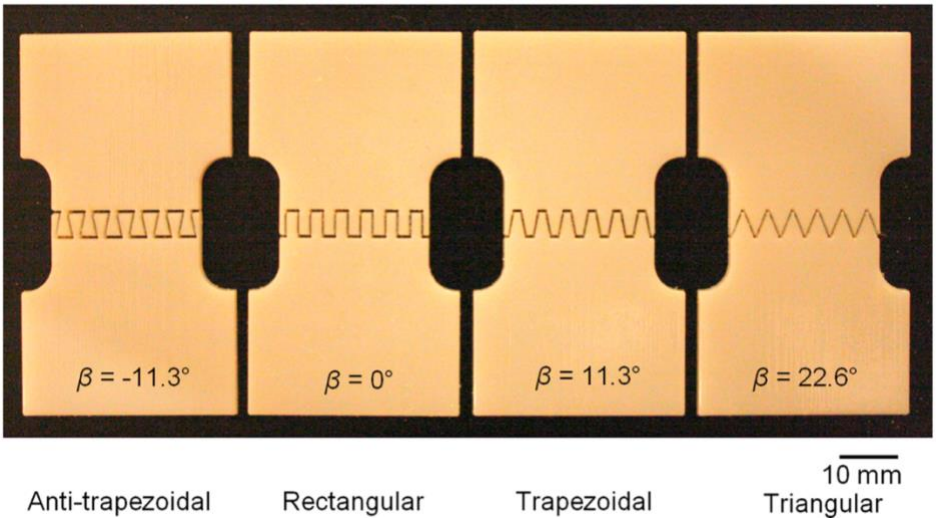

Figure 2.5. (A) 3D-printed samples with anti-trapezoidal, rectangular, trapezoidal and triangular geometries, in 10mm [86]. Reprinted with permission from Elsevier.

The stiffness, strength and toughness of the suture interface was found to be related to the geometrical parameters and the properties of the material, again as discussed in Section 2.3.2. Nacre shells.

Lin et al. suggest that an increase in soft Tango Plus can generate additional strain, and the smaller angle of tooth shape (referred to as the anti-trapezoidal) of the stiff scale's boundary increases the load transferred between the teeth, thus increasing the stiffness of the structure. Larger angles of the anti-trapezoidal shape may lead to tooth interlocking and increased ductile damage at the interface, which can improve the overall structural toughness [86].

2.3.2 Nacre shells

Shellfish structures with fine interface shapes have also been founded. Nacre is the famous biological hard tissue, which is beyond the reach of many modern ceramic materials [87]. The microstructure of nacre shell is shown in Figure 2.6, with calcium carbonate and soft organic polymer arranged in columns with some overlap, was widely concerned from researchers. These kinds of structure has various names, such as 'brick-and- mortar' [88, 89] structure or 'tablets-infill' [2, 75] structures, which have high strength and toughness mechanical. The following analysing section will use the term 'tablet' to refer calcium carbonate, term 'filler' to refer organic polymer.

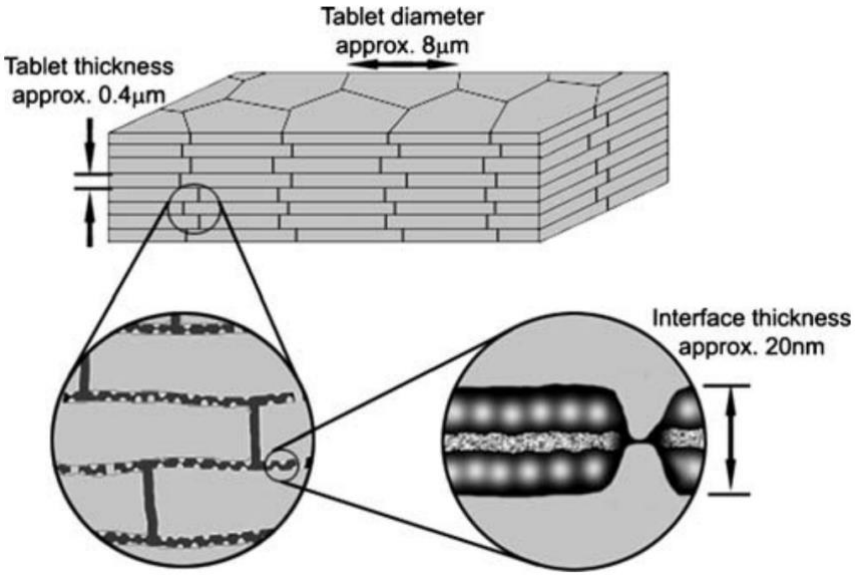

Figure 2.6. Structure of nacre shell [90]. Reprinted with permission from Springer Nature.

2.3.2.1 Toughening mechanisms in nacre shells

Song et al. believe that the toughening agent for nacre shells lies in the deflection of cracks, the removal of aragonite and the connection of organic bridges [91]. Crack deflection means that when the crack propagates perpendicular to aragonite tablets, it first extends along the organic tablets between the long interfaces of the aragonite tablets and then deflects again at the short interface to another organic tablet parallel to it [92]. The frequent deflection of the crack leads to an extension of the extension path, which can increase the absorption of fracture work, significantly increasing the resistance to extension and leading to an increase in external forces that toughening the material. Mirzaeifar et al. tested Objet Connex500 printed nacre-like structures by fracture toughness tests, using Vero White Plus and Tango Black Plus as the tablet and fillers, and concluded that the layered structure of such tablets could lead to defect tolerance properties [68].

Tablet sliding is a key mechanism for increasing the toughness of the nacre-like structure [2]. When the layers slide, the tablets squeeze against each other thereby increasing the sliding resistance. Tablet fracture often accompanies tablet sliding. The

fracture mainly occurs mainly in the middle of tablet, and the tablet that fractures remain in close contact with the filler at the long interface. The adhesion between the organic infill and the aragonite layer will prevent further crack extension, thus increasing the energy required for fracture and improving the toughness of the material [93].

The waviness or rough surface of aragonite tablets in nacre shells is another key feature in the hardening of layer structures [2, 4], as shown in Figure 2.7, where some aragonite tablets have a dovetail feature at the end. This structure produces progressive locking around the cracks and can withstand high tensile forces. The sliding mechanism causes lateral expansion and locking of the tablets possessing waviness, and promotes large-scale strain hardening.

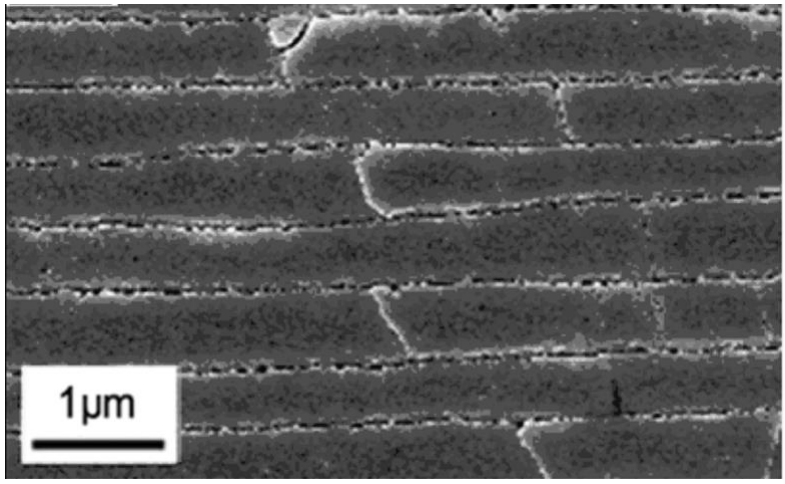

Figure 2.7. The scanning electron micrograph of the tablet [90]. Reprinted with permission from Springer Nature.

Barthelat et al. carried out tensile and shear tests on small nacre layer samples and demonstrated that shearing of the nacre layer was accompanied by significant transverse expansion [2]. Finite element modelling demonstrated that the waviness of the tablets produced strain hardening and that the dovetail shape provided a strong locking mechanism. Figure 2.8 shows the representative elementary volume (RVE) diagram of the stress distribution in a thin aragonite tablet with a dovetail under simulated tensile tests. The parallel aragonite tablets are locked to each other under

stress and show a large amount of stress hardening. The mineral bridges appear to be concentrated in the middle of the tablets, possibly strengthening the core region, and preventing delamination of the tablets. Espinosa et al. suggest that tablet sliding requires that the dovetail tablets should have 'bridges' to limit lateral expansion in the core region and that the filler material should be softer relative to the tablets so that the interface between the tablets enhances the toughness of the nacre-like layer structure, increase the viscoelastic energy dissipation [94].

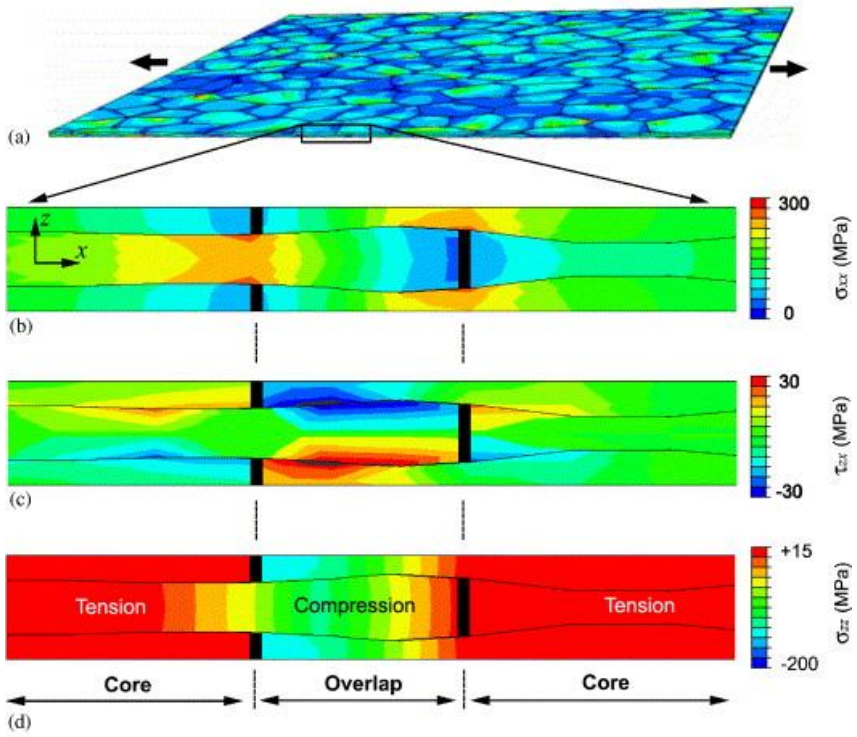

Figure 2.8. (A) The tensile stress response showing in representative elementary volume diagram. (B) Tensile stress in a single unit. (C) Shear stress is concentrated near the interface. (D) The out of plane stress shows compression in the overlap region and expansion in the core region[2]. Reprinted with permission from Elsevier.

The deformation mechanism of the nacre-like structure is multi-stage [95] and can be broadly divided into adhesion forces between the tablet and filler, sliding between the tablets and interlocking of the tablets. Dovetail shaped tablets used to simulate the waviness of real nacre aragonite have appeared in many studies [2, 75, 89, 93, 95, 96], using a variety of experimental and numerical methods to model this mechanism in synthetic composites.

Espinosa et al. produced tensile specimens of nacre-like structure with dovetail tablets through FDM printing methods using ABS to produce the tablets and epoxy resin to penetrate the interface gap between the tablets for use as a filler material. The energy dissipation and strength properties of the multi-material structure are 50% higher than flat tablet materials, which directly verifies the key role of induced tablet interface hardening [90].

Another key point for interface hardening is the overlap length of the tablets. It has been reported that high overlap ratio can improve hardening mechanism by making the tablet sliding region larger [75, 96, 97] and creating strong cohesive forces within the tablets. Djumas et al. did not observe this failure mechanism of similar tablet interlocking structure in the case of short tablet overlap with 2.6mm, but found this deformation mechanism in flat tablet composites with longer overlap length of 8mm [55].

Another consideration for achieving good hardening mechanism through nacre-like structures is the choice of constituent materials. The material of the tablet should be stiff and have a high tensile strength to prevent the tablet fracture during sliding. The filler between the tablets does not need to be hardened and should be made of a softer material than the tablet material thus can withstand high strains. Barthelat et al. considered small nacre layer specimens in the dry and in the hydrated conditions, respectively. The dry specimen implies that the organic filler loses its water become dry and stiff. The dry nacre layer specimens behaved like ceramic under tensile testing and failed in a brittle fashion. Specimens under hydrated conditions exhibit linear elastic behavior [90].

2.4 Auxetic structures

Auxetic structure usually refers to structures with negative Poisson's ratio. Poisson's ratio is the ratio between transverse strain and axial strain. Materials subjected to

uniaxial tension usually contract in a direction orthogonal to the applied load. A material with a negative Poisson's ratio will expand in the transverse direction [98].

Some researchers have proposed periodic 2D geometries to achieve negative Poisson's ratio structures [98, 99]. Hexagonal honeycomb structures are commonly found in the core of sandwich structures, with high stiffness and flexural resistance. Honeycomb structures have been shown to have superior energy absorption properties in both 2D [100] and 3D metamaterial [101] structural studies. honeycomb structures have excellent energy absorption properties. When the lattice tension in-plane, the hexagonal honeycomb structure has a positive Poisson's ratio. Lakes [100] that structures with internal raised microstructures expand in the direction of the vertical force during tension. When the hexagonal honeycomb is reversed, the direction of the vertical force becomes expanded during tension, with less deformation and show negative Poisson's ratio values. Whereas the reversed internal raised honeycomb structure shown in Figure 2.9 is similar to the dovetail feature discussed in Section 2.3 Nacre shells, the negative Poisson's ratio does not appear to have been analyzed in the study of dovetail feature tablets.

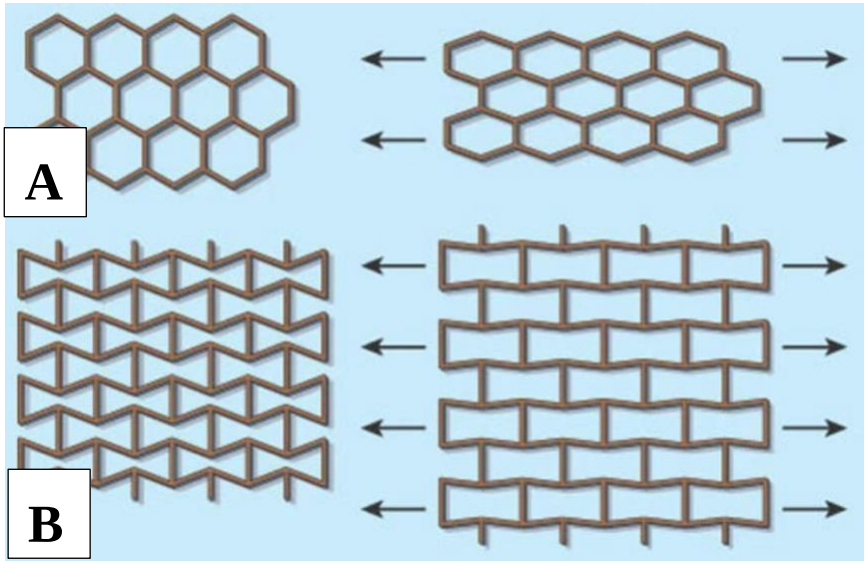

Figure 2.9. (A), (B). Hexagonal honeycomb structures and inverted honeycomb structures sketch and deformation during tension [100]. Reprinted with permission from Springer Nature.

Chapter 3

Materials and Methodology

3.1 Experimental overview

This chapter describes how multi-material structures based on the nacre were designed, 3D printed and tested. A FDM dual 3D printing method was used to produce bio-inspired, multi-material structures. Stiffer polylactic acid (PLA) was chosen as the tablet material and flexible thermoplastic polyurethane (TPU) as the filler material. This combination structures are proposed to improve the mechanical properties of 3D printed parts to obtain a good balance of strength, stiffness, and toughness. Tensile tests, cyclic tensile test and fracture toughness tests are used to measure these properties.

3.2 Experimental preparation

3.2.1 3D printer and materials selection

The project was be completed using an Fused Deposition Modelling (FDM) type printer for dual material printing. The M2 Dual 3D printer from MakerGear has two extruders allowing printing with two different filaments at the same time. The 3D printer with filaments on are showing in Figure 3.1.

To simulate nacre layer with stiffness and strength of brittle tablet, polylactic acid (PLA) was chosen as the tablet material and thermoplastic polyurethane (TPU) as the soft material to represent the soft organic filler due to its high elongation and flexible.

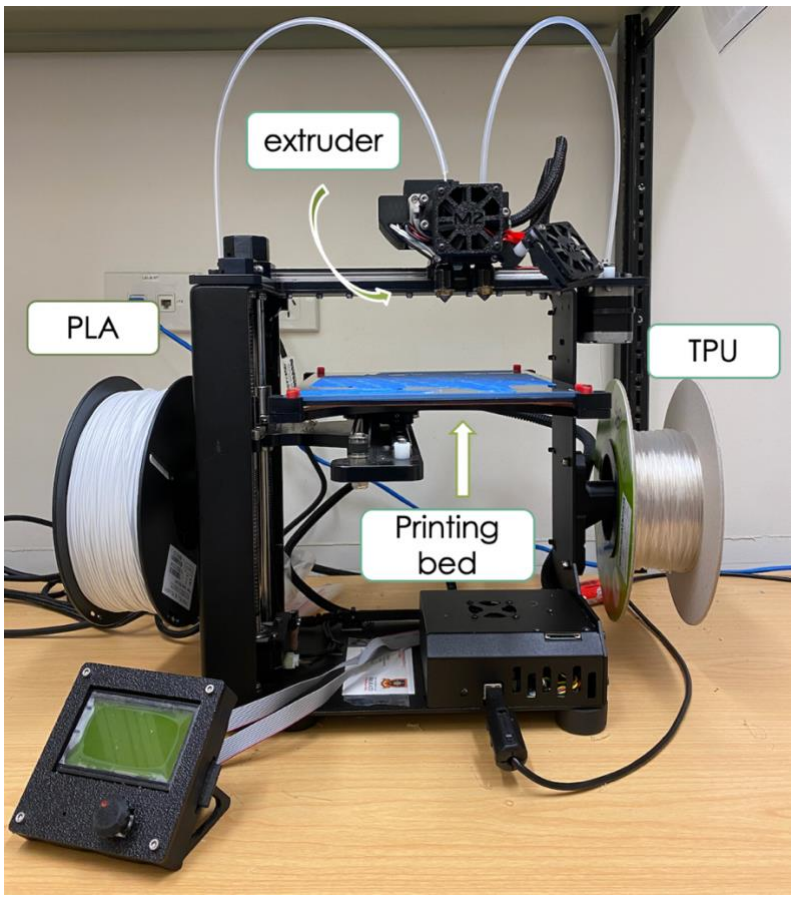

Figure 3.1. MakerGear M2 dual 3D printer.

Trial printing was carried out determine the printing parameter and smallest tablet size. Black 1.75mm PLA for trial printing was sourced from MakerGear [102]. White 1.75mm PLA for formal printing was sourced from Shenzhen eSUN. Ltd [103]. The natural colour 1.75mm TPU was sourced from Imagin Plastics. Ltd [104]. The reported properties and recommended printing parameter are shown in the Table 3.1.

Table 3.1. Filament technical parameters and properties [102-104].

Filament type	Print temp (℃)	Bed temp (℃)	Density (g/cm^3)	Tensile strength (MPa)	Elongation at break (%)	Izod impact strength (KJ/m^2)
Black PLA	215-220	60-80	1.25			
White PLA	190-210	60-80	1.25	65	8	4
TPU	200-240		1.16	26	660	4.2

3.2.2 Geometry design

The design of multi-material nacre-like structures was based on Rim et al. [75] and Espinosa & Barthelat [74]. The multi-material layer structure uses as the dovetail interlocking structure. This structure was inspired by the microstructure of the nacre, where the waviness features gives the tablet an interlocking deformation mechanism.

All multi-material structures were designed and prepared using the SolidWorks software, and the models and unit volume ratios of the multi-material structures are shown in Figure 3.2 and Figure 3.3. According to the design steps proposed by Barthelat [2] to optimize the interlocking structure, the aspect ratio and overlap ratio of a single dovetail tablet will follow the principle of the higher the better to maximize the sliding region.

In the current work, the inclination angle θ of the middle narrow section will be used as a variable by adjusting the interlocking dovetail angle to study the effects of different dovetail angles on the interlocking deformation mechanism. The dovetail angles is 1˚, 3˚, 5˚ and 9˚ respectively. Flat tablets with a 0˚ dovetail angle will also be investigated for comparison. All tablets will be keep at a constant length L of 16 mm and a width W of 2 mm (2.5 mm for 9˚, the that minimum thickness of the tablet is no less than 1mm, limitations due to printer resolution). The overlap ratio of the tablets will be approximately 0.5 and gap t between the tablets will be filled with flexible material TPU. The specific pattern features will be discussed in Section 3.3 3D printing.

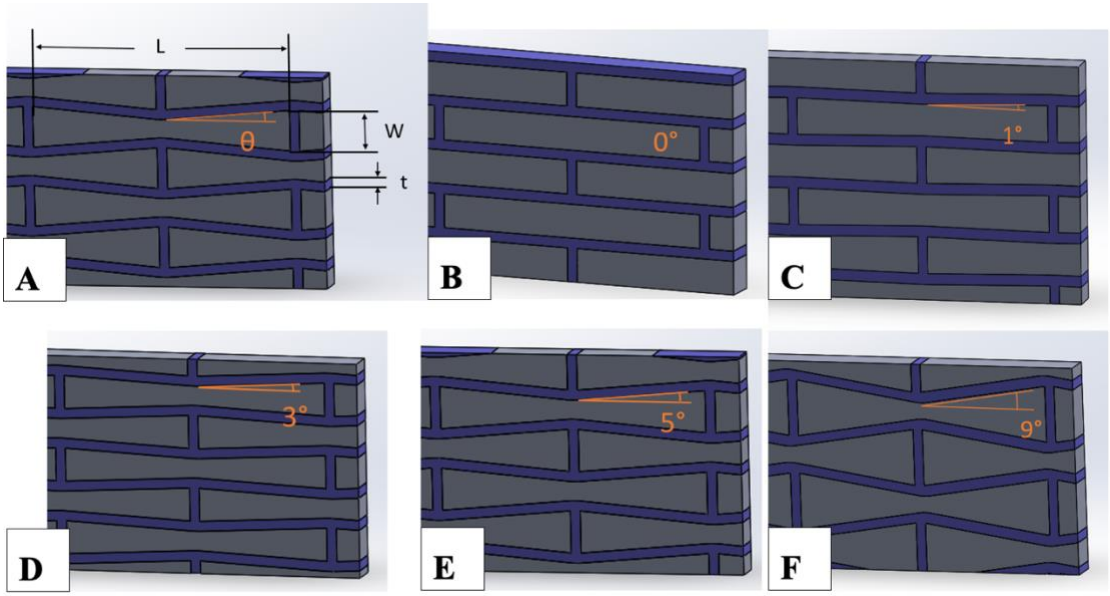

Figure 3.2. (A) Periodic patterns structure with geometric parameters. (B), multi-material structures with dovetail angle 0˚. (C),1˚. (D), 3˚. (E), 5˚. (F), 9˚. All sketches were through SolidWorks software.

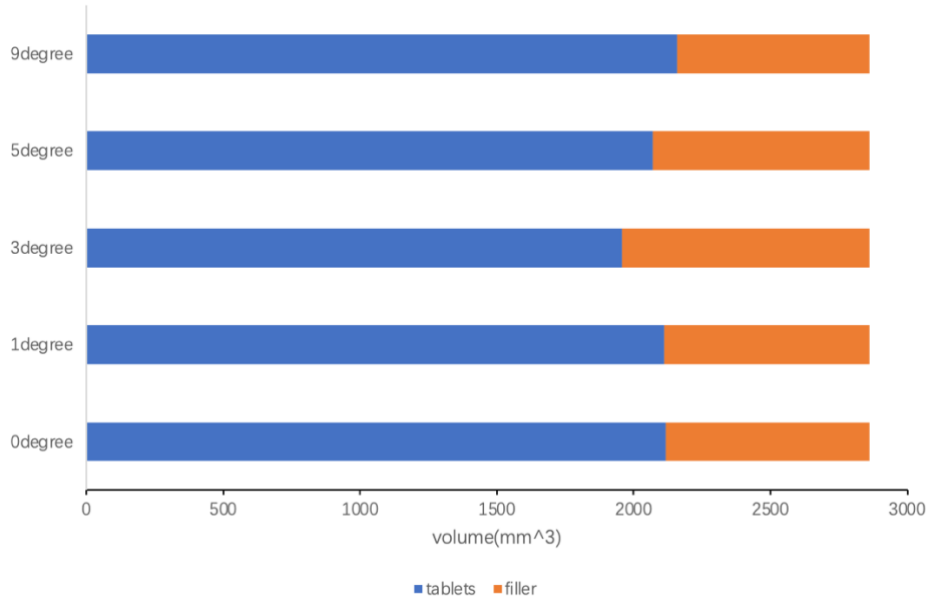

Figure 3.3. Tablets (PLA)/ filler (TPU) volume ratio for various dovetail angles of multi-material structures.

3.2.3 Tensile test preparation

Tensile tests were carried out based on ASTM D638-10: Standard Test Method for Tensile Properties of Plastics. The initial plan for 3D printed tensile specimens was to follow the ASTM D638 method. In practice, due to the small size of the tablets and

difficult printing TPU, the printing speed was 900 mm/min and the time required to print a dog-bone specimen was 1 h 50 mins. To save time and material, it was decided to print only narrow sections and to reduce the thickness of the specimen, using acrylic sheets as tabs at both ends. The acrylic sheets will be fixed with epoxy resin (Araldite Super Strength from Selleys, Australia). The details are shown in Figure 3.4 and Table 3.2, where L_t is the length of tensile test sample, w_t is the width of sample and t_t is thickness of sample.

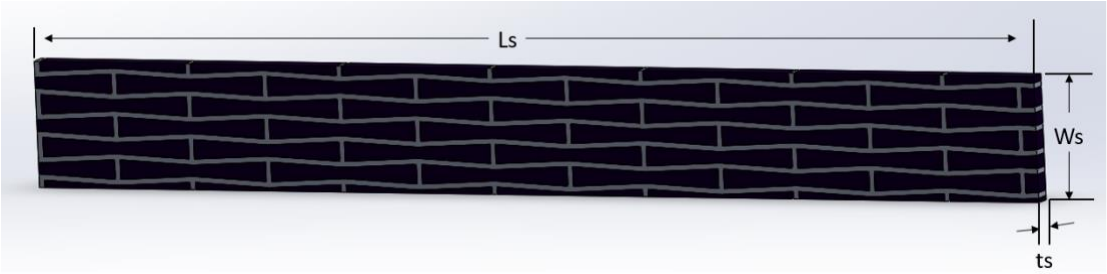

Figure 3.4. Parameter of tensile test specimens.

Table 3.2. Tensile test specimen and acrylic tab parameters.

L_t	110mm
w_t	13mm
t_t	2mm
Length of tabs	25mm
Width of tabs	19mm
Thickness of tabs	2mm

3.2.4 Fracture toughness test preparation

The fracture toughness tests was based on ASTM D5045-14 standard test methods for plane-strain fracture toughness and strain energy release rate of plastic materials. The single-edge-notch bending (three-point bending) method and the compact tension (CT) method are both standard methods for measuring fracture toughness [70]. Single-edge-notch bending (SENB) test is used in this project. Unlike tensile specimens, the

specimens used in the fracture toughness test have prefabricated fatigue cracks to simulate micro-cracking defects in the actual component, as shown in Figure 3.5. The parameter for SENB specimen is showing in Table 3.3, where the crack length a ranges from 0.45< a/W < 0.55.

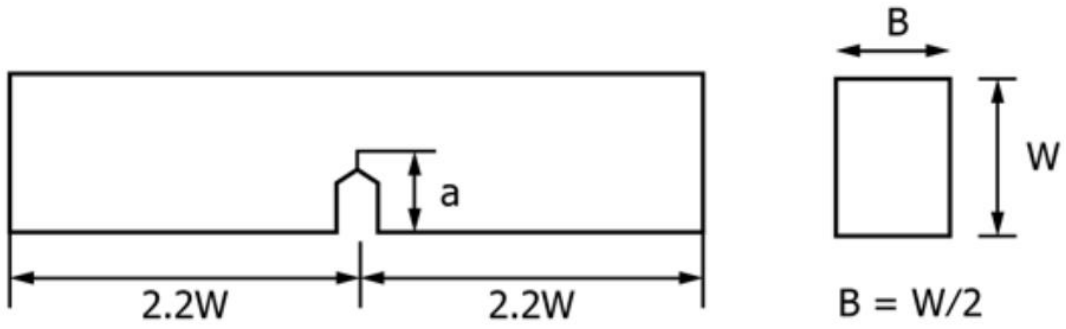

Figure 3.5. SENB specimen from ASTM standard D5045-14 [70].

Table 3.3. Parameter for the geometry of fracture toughness specimens.

Width (W)	10mm
Thickness (B)	5mm
Length (4.4W)	44mm
Crack (a)	4.5-5.5mm

3.3 3D printing

Although 3D printing technology can carry out rapid and fine manufacturing, it is necessary to determine appropriate printing parameters through trial prints. Therefore, many trial prints were conducted to determine the print parameters and whether the material printed well. In previous studies of 3D printed, nacre-like, multi-material structures, the width of the tablets was under the 5 mm range [68, 75, 95]. To maximize the aspect ratio of the tablets and achieve an overlap ratio close to 0.5 [74], trial prints were also required to determine the minimum print size for the narrow middle section of the tablet and the soft organic filler because of the limitations of the printer resolution. Figure 3.6 shows photographs of the 27 trial prints.

The overall print quality is strongly influenced by the bonding between the print materials, the print speed, the outline profile and the nozzle temperature. The nozzle temperature is set to 215 °C and the print bed temperature to 80 °C, which prevents unnecessary distortion of the specimen during cooling. PLA/ TPU multipliers indicate the mass flow of the filament, increasing the multiplier will increase the extrusion capacity of the filament.

Trial printing black PLA specimen shows that even 1˚ can be printed by a 0.35mm nozzle diameter print extruder. With extrusion multiplier being 1.05 for PLA and 1.5 for TPU, a width of 0.4mm of TPU between PLA tablets can be printed, but the PLA will be joined together and the TPU filaments are very thin and hidden between the PLA and not visible. After adjusting the extrusion multiplier of the PLA to 0.9 and the extrusion multiplier of the TPU to 1.7, the 0.6mm TPU can be shown clearly.

When printing with the above extrusion multipliers, white PLA was not printed as effectively. 18 more trial prints were conducted to eliminate the air gap between the white PLA and TPU as shown in Figure 3.7 (A). The TPU filament stopping printing usually happened during the printing process. As shown in Figure 3.7 (B), the TPU was

blocked in the channel between the printing extruder and the filament feeder, probably because the speed of printing was too fast for printing TPU through a narrow nozzle. The printing speed also affects the print quality. Low print speeds improve print quality but are less time efficient. Therefore, it is important to adjust a reasonable speed. The overall printing speed is 900 mm/min and the print speed for the first layer is set at 50% of the overall printing speed. To improve the surface finish of the printed parts, an outline profile is created in the print. The outline underspeed can be adjusted so that the outermost perimeter speed is reduced to improve the surface finish of the model without reducing the overall printing speed. Solid infill underspeed are usually faster than any other part of the print, it has to be percentage reduced from overall printing speed to prevent the printer itself from vibrate when filling thin-walled gaps [105].

The final print parameters and pattern sizes for the 3D printed, multi-material, dovetail angle structure was determined as shown in Figure 3.7 (C) and Table 3.4, respectively.

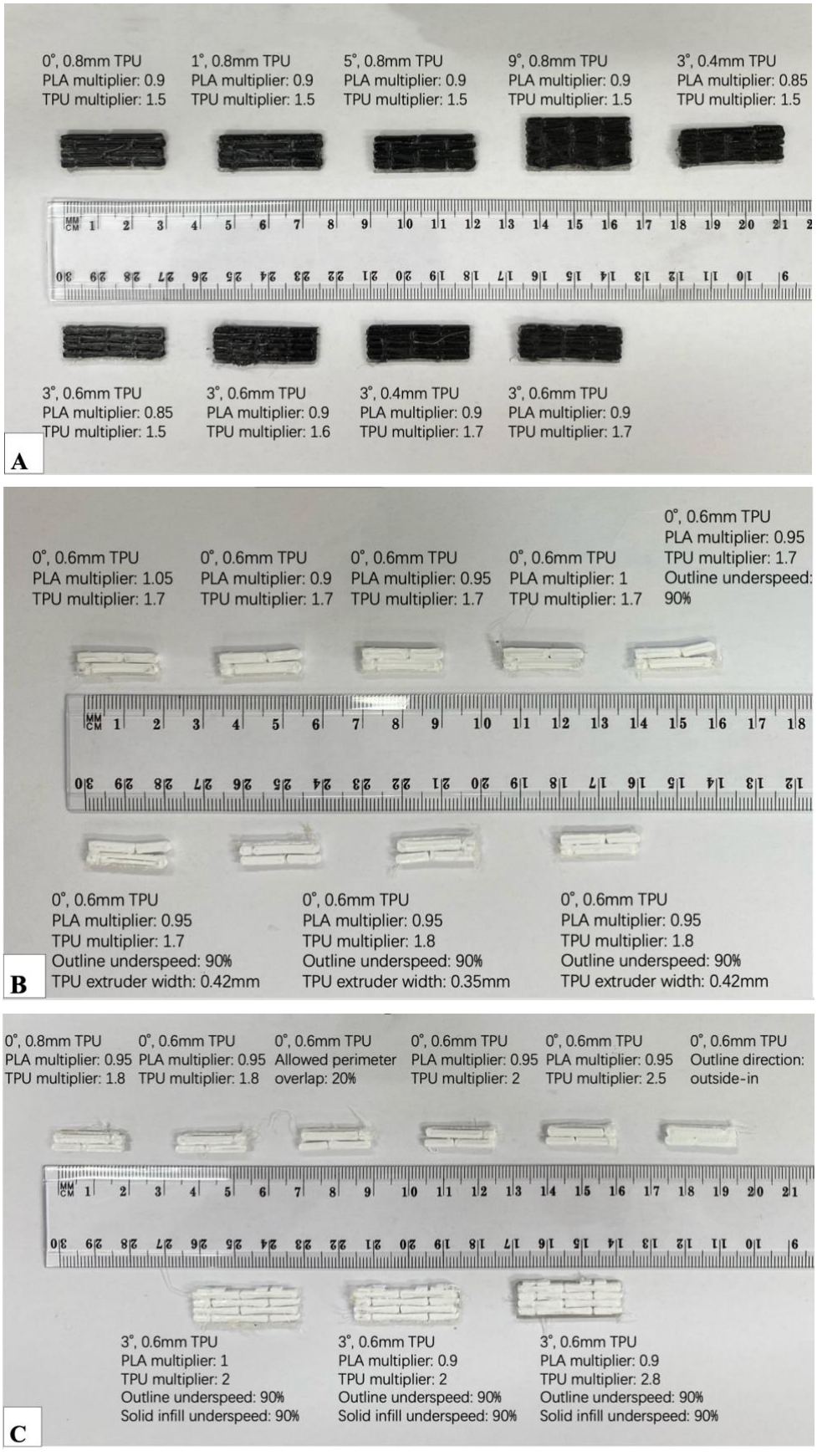

Figure 3.6. (A) Trial printing with black PLA. (B), (C) Trial printing with white PLA.

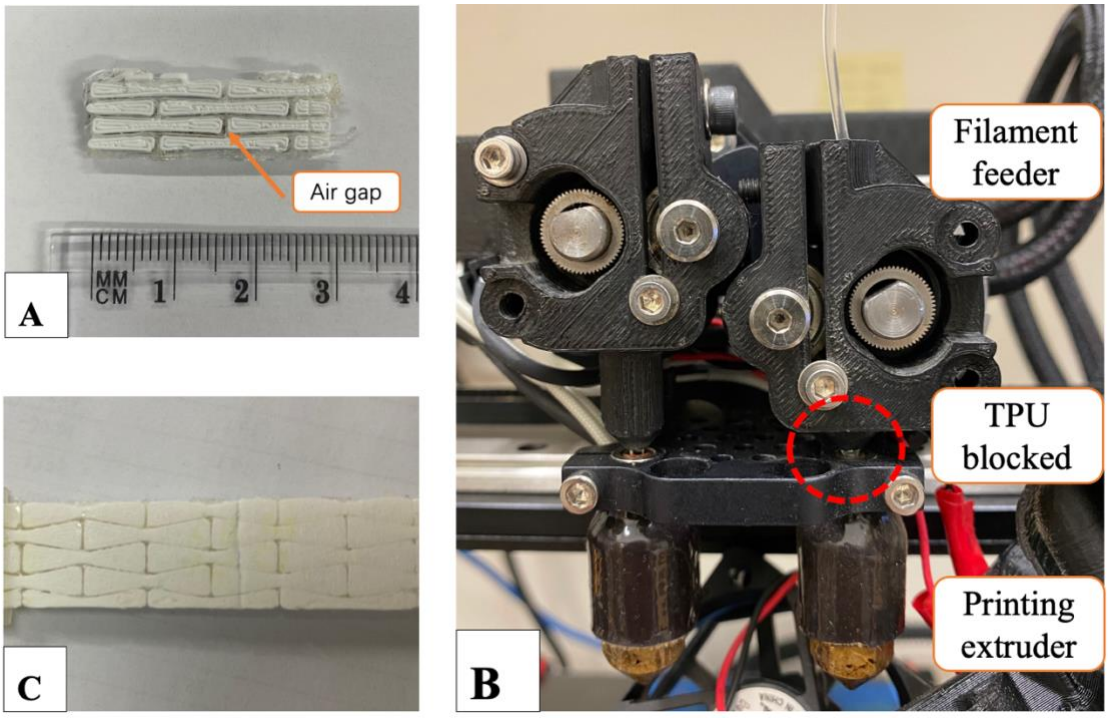

Figure 3.7. (A) Air gap between PLA and TPU. (B) TPU blocked between filament feeder and printing extruder. (C) Final printing settings printed PLA & TPU structure.

Table 3.4. Final printing parameters and geometric pattern parameters.

PLA multiplier	0.9
TPU multiplier	2.8
Outline underspeed	90%
Solid infill underspeed	90%
Length of tablet (L)	16mm
Width of tablet (W)	2/ 2.5mm
Dovetail angle (θ)	0˚-9˚
Thickness of filler (t)	0.6mm
Thickness of narrow section (t_0)	0.4mm

3.4 Mechanical testing

In order to determine the influence of dovetail angle on the mechanical performance of multi-material structures, tensile tests, cyclic tensile tests and fracture toughness tests were carried out in the experimental section to analyze the special mechanical response under loading, which will be discussed through tensile strength, yield strength, energy absorption properties and other parameter and criteria.

3.4.1 Tensile testing

All tensile testing of the printed multi-material dovetail structure specimens were performed using the universal testing machine 100kN Tester (5982 from Instron, USA) with a 5kN load cell shown in Figure 3.8A. A smartphone (iPhone 11Pro from Apple, USA) was used for videoing acquisition during the tensile tests. The experiments were loaded with a crosshead displacement rate of 5mm/min according to ASTM standards. Strain was measured using 25mm extensometer fitted the samples. All 3D printed, multi-material specimens were tested four replicates of each sample until the displacement was 20 mm, one replicate specimen was tested to complete break.

In order to reduce the actual printing time and to assist gripping the specimen in the test apparatus, four laser cut acrylic plates were used as specimen support tabs each, two on either face of the planar specimen and glued by epoxy resin. Sandpaper is used to roughly abrade the acrylic tabs to ensure optimal adhesion of the epoxy resin and epoxy resin was allowed to cure for 48 hours. Support tab holders were used for positioned that all samples had the same effective length, shown as Figure 3.8 B,C. All specimens were put in constant climate chambers (KBF 115 from Binder, Germany) at 23℃ and 50% relative humidity for over 48 hours before testing.

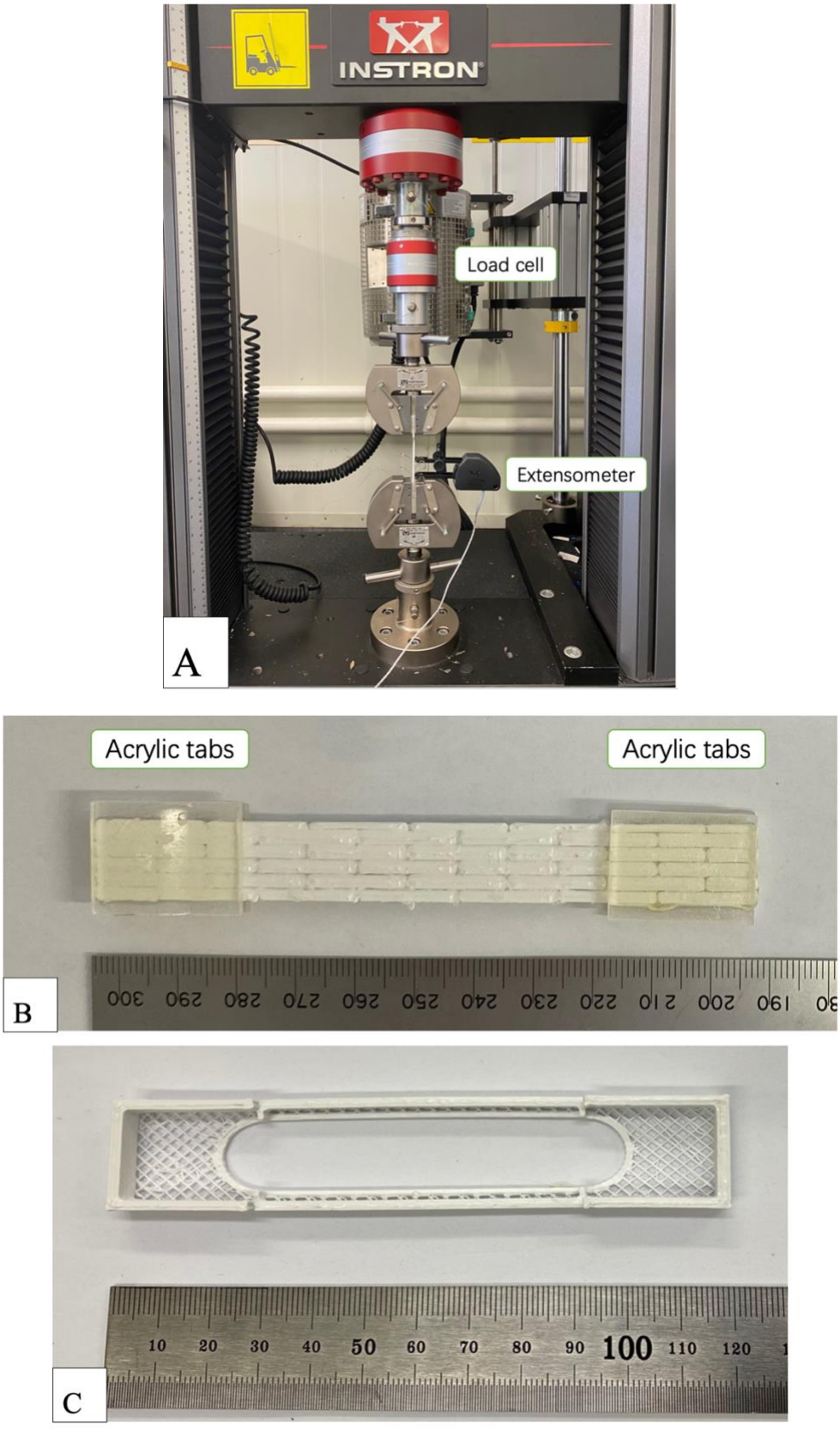

Figure 3.8. (A) Instron 100kN tester with 5kN load cell during tensile test. (B) multi-material with 1˚ dovetail tensile specimen with acrylic tabs. (C) Tab holders.

3.4.2 Cyclic tensile test

Based on the results of tensile test shown in Section 4.1, the multi-material structure shows the multi-stage and non-linear mechanical behaviour during tensile test. Structure with different dovetail structures show the distinct plateaus (inflection points) with same tensile stress at the beginning of the tensile curve. Considering the possibility of a yield plateau, cyclic tensile tests were carried out to see what happens to the multi-material structures with dovetail 0˚ and 9˚ in the plateau region of the tensile curve when repeatedly loaded and unloaded. The experimental method for the cyclic tensile tests is same with the formal tensile test based on the ASTM D638-10 method.

The experiment procedure has the the following additional experimental setup. There are 5 cyclic loading conditions with 5 repetitions for each cycle was subjected to specimens, then do the tensile test and stopped at displacement of 20mm at final step, as shown in Table 3.5.

The range of Cycle 1 is between 0 to 0.8MPa, corresponds to the first elastic stage shown in figure 4.2 tensile stress-strain curve. The stress range for Cycle 2 includes the plateau range to capture damage and mechanical properties close to the yield point. The range for Cycle 3 is the tensile stress before the ultimate tensile strength (UTS) point. The range for Cycle 4 and Cycle 5 is strain based, strain 2.7% In the tensile test, the sample with dovetail 0˚ has reached the UTS point at a strain of 2.7%, while the 5˚ dovetail sample had not yet reached it. The purpose of this cycle is to check the mechanical response of the dovetail 0˚ sample during the UTS. Cycle 5 is set to check the secondary strain hardening response in Section 4.2.1.3.

Table 3.5. Cyclic tensile test procedure.

	Range	Repetitions
Cycle 1	Tensile stress from 0MPa to 0.8MPa	5
Cycle 2	Tensile stress from 0MPa to 1.5MPa	5
Cycle 3	Tensile stress from 0MPa to 4MPa	5
Cycle 4	Tensile strain from 0% to 2.7%	5
Cycle 5	Tensile strain from 0% to 4.2%	5
Stage 6	Displacement extension to 20mm	

3.4.3 Fracture toughness

The fracture toughness test of 3D printed multi-material specimens was also conducted by universal testing machine 100kN Tester (5982 from Instron, USA) equipped with 5kN load cell. The crosshead displacement rate with 10mm/min was applied to specimens. Figure 3.9 (A) shows the fracture toughness test set up with loading rigs and supporting pins, Figure 3.9 (B) shows the fracture toughness test specimen with notching.

Due to the small size of the fracture toughness specimens, the prefabricated cracks cannot be cut using a standard notching machine, instead a hacksaw is used to make the notch and the cracks are sharpened by a fresh knife blade. Pre-test conditions was same as tensile test, contain with temperature in 23℃ and humidity in 50% RH for 48+ hours.

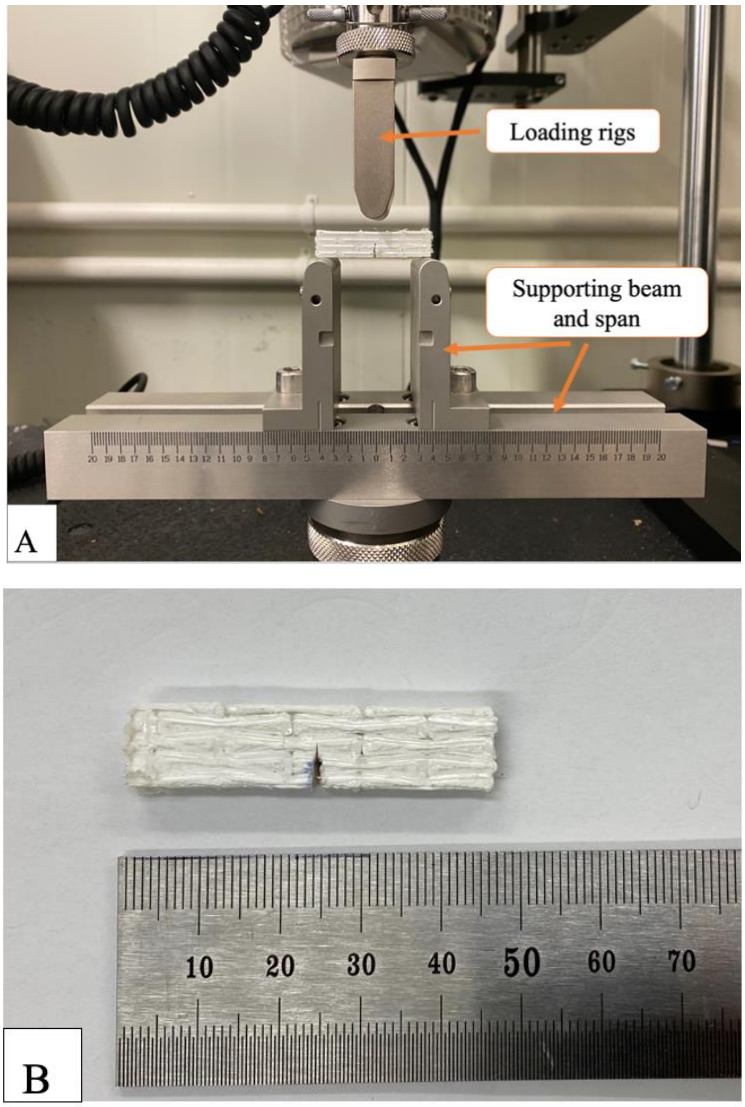

Figure 3.9. (A) Fracture toughness test set up. (B) Fracture toughness specimen with notching.

Linear elastic fracture mechanics suggests that the component is safe when the stress intensity factor $K < K_{IC}$ at the tip of the crack, when $K = K_{IC}$, the component is in a dangerous critical state, and when $K > K_{IC}$, the crack will expand unstably [106]. The key to determining K_{IC} is to determine the ultimate load P_Q value that the specimen can withstand at the time of unstable crack growths. The value of P_Q can be determined from the diagram shown in Figure 3.10.

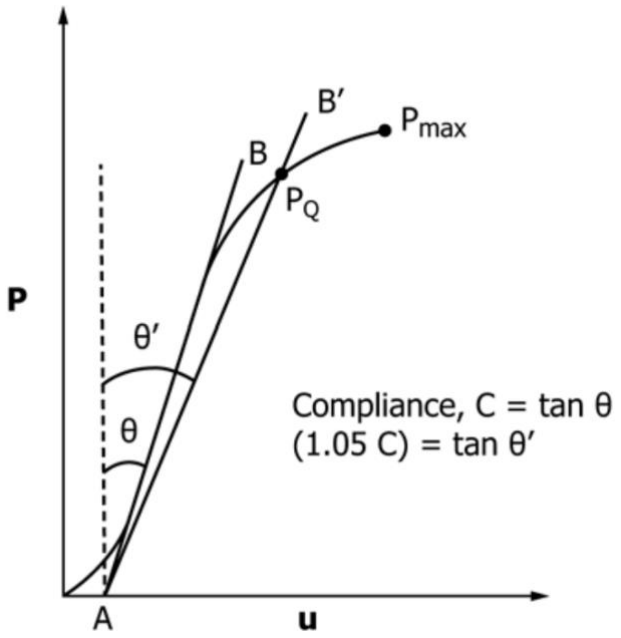

Figure 3.10. Diagram to determine the C and P_Q, axis unit U is displacement [70].

The experiment requires that the slope of the line AB be determined from the test results by plotting the slope of the line, the reciprocal of which is the initial compliance C. The second line, AB', is 5% more compliant than the line (AB), from which the line AB' can be plotted .

The ASTM standard [70] requires that if the maximum load P_{MAX} of the specimen falls within the line AB and AB', P_{MAX} can be used to calculate K. If P_{MAX} falls outside the line AB and the line AB', the intersection of the line AB' and the load curve is used as P_Q. If the ratio of P_{MAX} to P_Q is less than 1.1, P_Q is used in the calculation of K_Q. However, if the ratio of P_{MAX} to P_Q is bigger than 1.1, then the test will be invalid.

Chapter 4

Results and Discussion

4.1 Tensile Results

The tensile test results for the 3D printed, nacre-like, multi-material structure specimens are shown in Figure 4.1. All specimens exhibited multi-stage fracture, for specimens with a dovetail angle of less than 3˚, the stress-strain curve shows five stages: elastic region, yield plateau, strain hardening, interface damage and flexible material elongation. For multi-material structure specimens with dovetail angles of 5˚ and 9˚, the graph lines show 6 stages with addition of a secondary strain hardening stage.

To investigate the effect of soft filler pattern on hardening mechanism of nacre-like multi-material structures, PLA was used as both the tablet material and filler material, and specimens were printed under the names ‘dovetail PLA & PLA’. Single-material unidirectional tensile specimens of pure PLA were also printed for comparison. Figure 4.2 illustrates the tensile curves for pure PLA specimen and dovetail PLA & PLA with 0˚ and 5˚ dovetail specimens, both structures show a fracture property of brittle material with high stiffness and modulus but insufficient toughness. The tensile strength and Young’s modulus for all specimen during tensile test is showing in Figure 4.3. The Young’s modulus of the specimens was calculated from the linear region before reached the UTS point because some of the specimens had a plateau stage in curve.

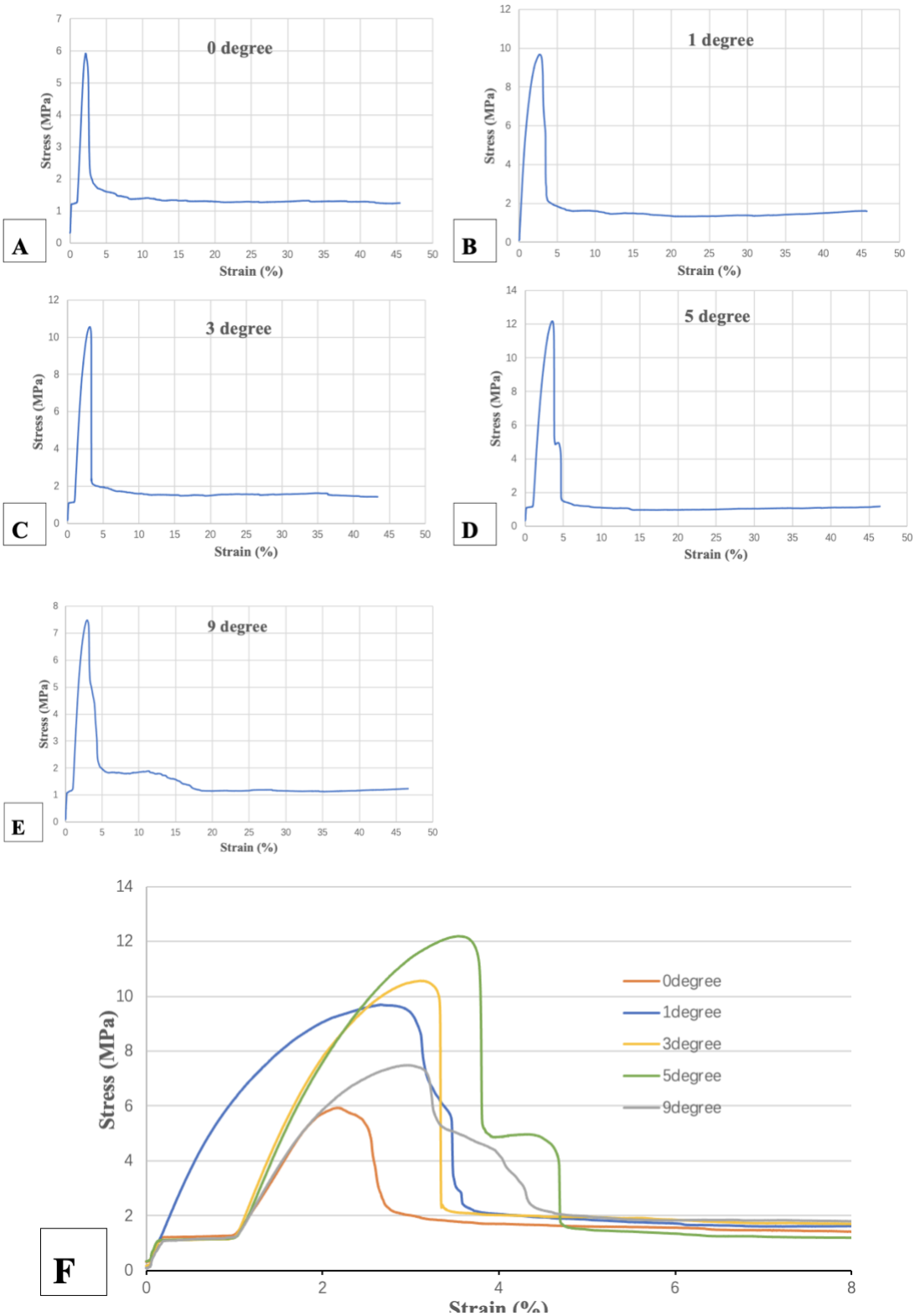

Figure 4.1. Tensile stress- strain curve of 3D printed, multi-material PLA & TPU structure specimens with dovetail angle (A), 0˚. (B), 1˚. (C), 3˚. (D), 5˚ and (E), 9˚. (F) Stress- strain curve up to 8% strain.

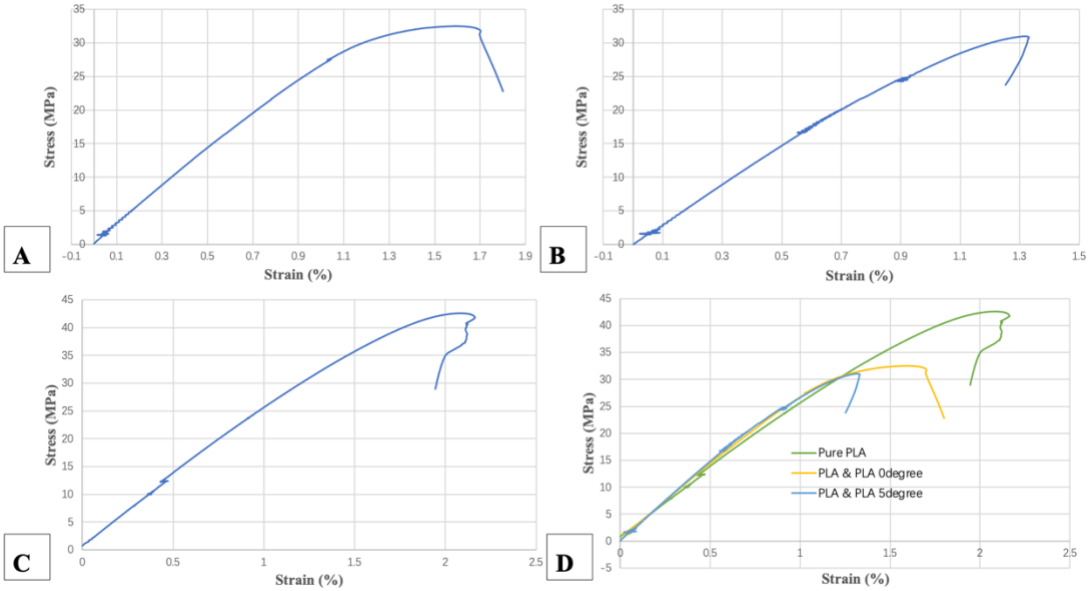

Figure 4.2. Tensile stress-strain curve of dovetail PLA & PLA multi-material structure with (A) 0˚ and (B) 5˚ dovetail specimens. (C) Stress- strain curve for unidirectional pure PLA tensile specimen. (D) Stress-strain curve comparison.

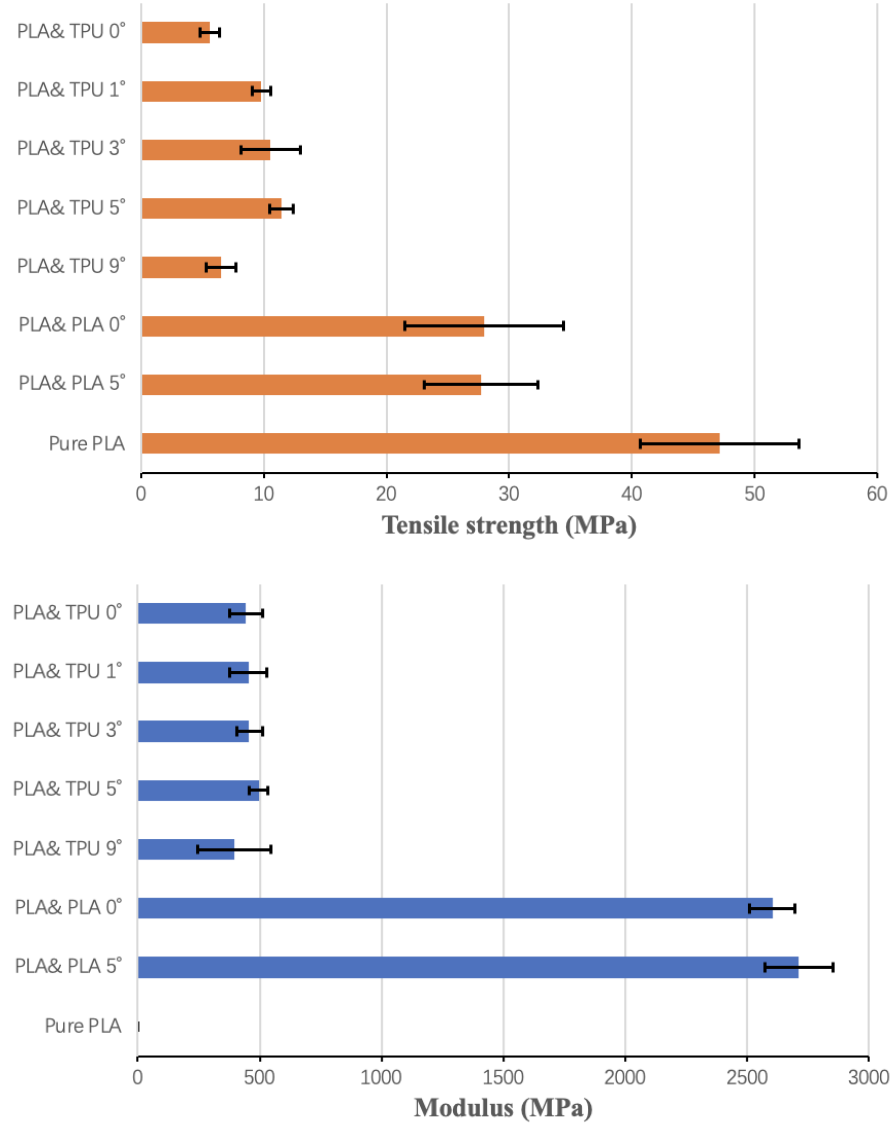

Figure 4.3. Ultimate tensile strength and Young's modulus from tensile testing of multi-material, dovetail structures and pure PLA specimens. Error bars are standard deviation.

4.1.1 Tensile test results calculation

Due to the size limit of strain gauge, the area where the tablet is pulled out may be outside the strain gauge during the tensile process of 3D printed, multi-material structure. Figure 4.4 shows the un-measurable and measurable interval sample during the test. When the tablets pull-out occurs outside the strain gauge, the strain data

recorded by the machine will not be the right value, the actual strain needs to be calculated by measuring the displacement change in the recorded screenshot.

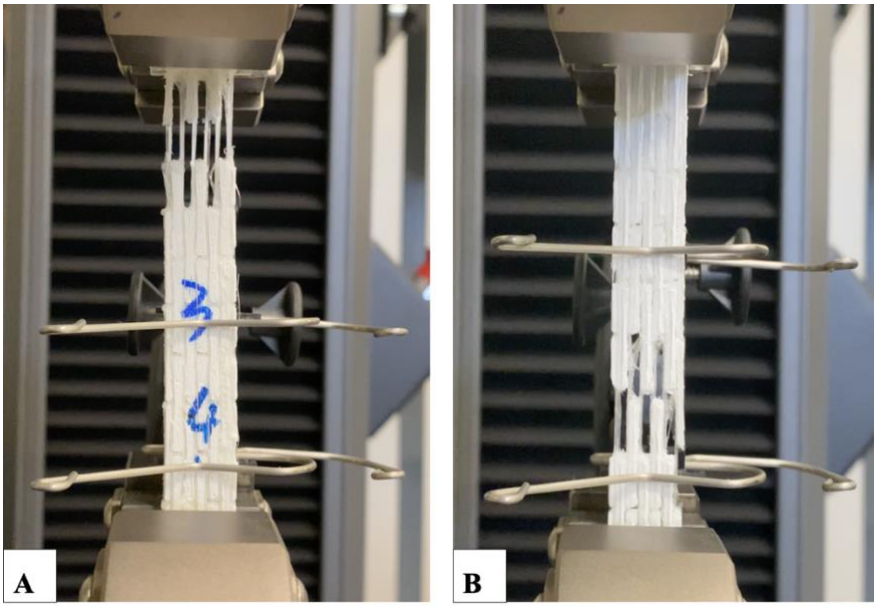

Figure 4.4. (A) strain gauge with un-measurable interval. (B) Strain gauge with measurable interval.

The specific calculation process was as follows: screenshots were selected for times of 0s, 60s, 120s, 180s and 240s (after start of elongation), inserted into an Excel sheet and measured the displacement through the screenshots. The lengths between holding grips were known and the actual displacement at these tensile times could be calculated from the ratios, which in turn gave the ratio of time to tensile displacement and ultimately the actual strain values.

4.2 Tensile testing stress-strain relationship

Stress-strain curves for dovetail PLA & PLA with 0˚ and 5˚ dovetail specimens and pure PLA tensile specimens show a single stage. The stress-strain curves for the multi-material structure show multiple stages, the combination of stiff and soft material provided sufficient modulus difference to produce complete interface broken, which is key to obtaining multi-stage deformation [95].

The softening stage of the multi-stage corresponds to the tensile deformation of the soft material at the short interface, while the hardening stage corresponds to the shear deformation of the soft material along the long interface. In 3D printed composites, this softening followed by hardening deformation behaviour has been reported in studies of 3D printed, multi-material structures that are influenced by boxfish skin interlocking structures [86] and other nacre structures [75, 95].

The tensile profile of the multi-material structure can be divided into six stages. The tensile curve with stages for the 5˚ dovetail structure is shown in Figure 4.5 (A). During the tensile process, the specimen shows mostly elastic deformation at first, after which the short interface between the end of the tablet and the filler first yields, resulting in the stress-strain curve reaching a yield plateau and reaching Stage 2. The short interfaces and long interfaces are shown in Figure 4.5 (B). This is followed by shear deformation and interlocking between the tablet and filler, leading to hardening Stage 3. With further tension, the interlocking mechanism fails showing Stage 4 and then the long interface between TPU and PLA fails as shown in Stage 5. Finally Stage 6 is the elongation of individual TPU filaments from the long surface until complete fracture. The details of the mechanical response will be discussed in the following sections, with name of First elastic stage, Plateau stage, Strain hardening, Long interface broken and Flexible TPU filler elongation.

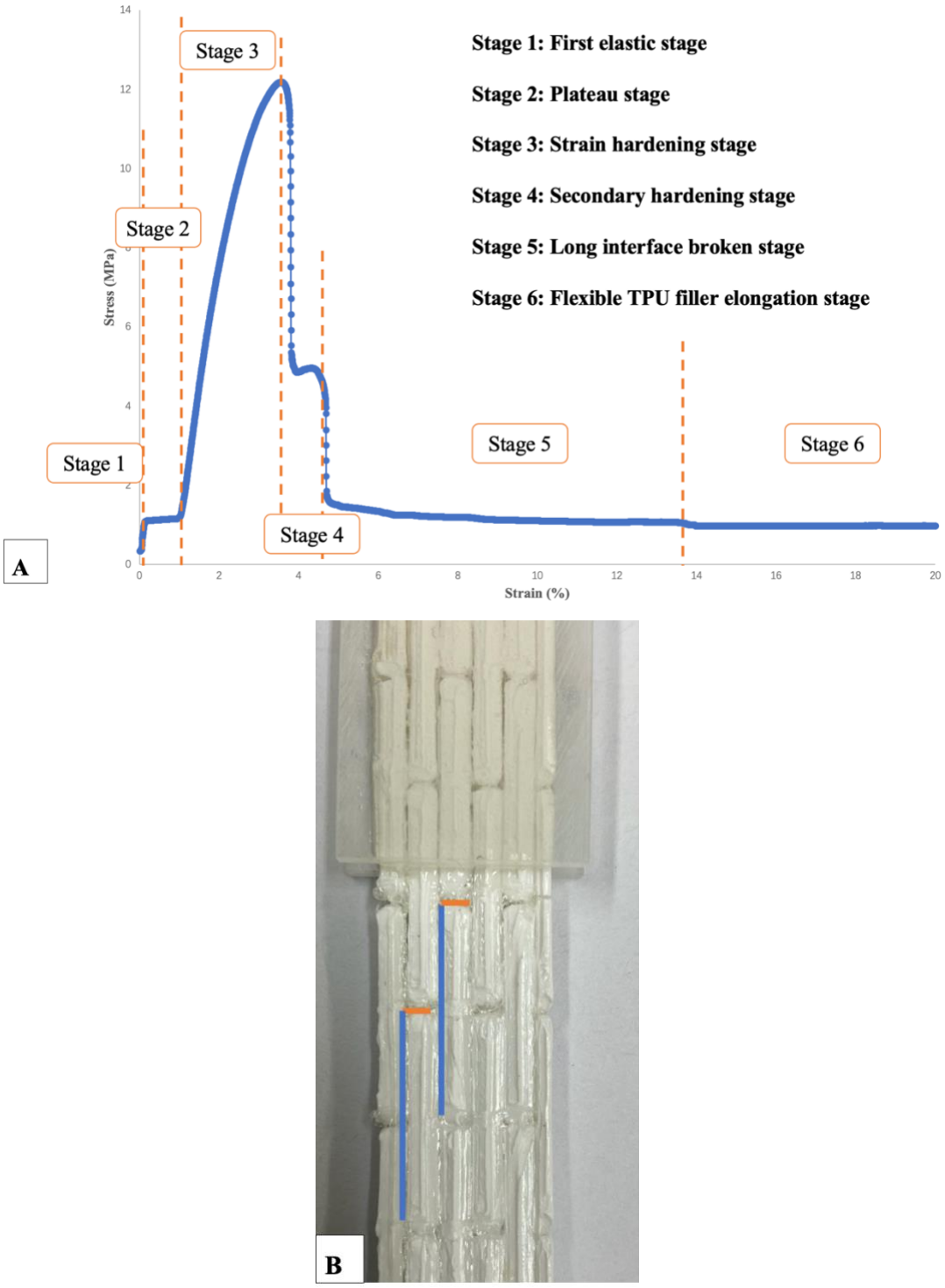

Figure 4.5. (A) Stress-strain curve up to 20% strain of multi-material PLA & TPU structure with 5° dovetail showing 6 stages. (B). Short interface in orange colour and long interface in blue colour.

4.2.1.1 First elastic stage

The results of tensile and cyclic tensile tests all shows that the first stage is the linear elastic stage, where the multi-material structure starts to be stressed and most of elastic deformation occurs. The stress is proportional to the strain and obeys Hooke's law. The end of this stage is the plateau stage.

4.2.1.2 Plateau

When the tensile stress reached the 1 MPa (varying by no more than 0.1 MPa), the plateau stage occurs in stress-strain curve for all multi-material specimens, and strain of the plateau was consistent on duration. Multi-material structures with 1˚ dovetail does not show the plateau during the testing, extra repeat samples were tested but only 1 of 8 samples shows the plateau. The initial test of five tensile specimens with multi-material dovetail 1˚ structure did not show a plateau during the test, additional replicates were tested, but only one of the eight samples showed.

The initial rise and fall of stress in the nacre-like structure was considered to be related to interface adhesion [75]. Once the adhesion between the tablet and the filler is overcome, the short interface will break. This is borne out by the results of tensile specimens of 3D printed unidirectional pure PLA and dovetail PLA & PLA which show no plateau region. Considering plateau stage may cause by the yield occurs, cyclic tensile tests were carried out to confirm see Section 4.5 Cyclic tensile test.

By comparing the different aspect ratios of nacre-like, multi-material structures [75, 95], there was no significant plateau showing in the results, which may be since the width of the tablets remained the same for all specimens in this experiment. Ko et al. determined the bonding force between FDM printed PLA and TPU in nacre-like, multi-material structures, the simulation and actual tensile results shows that the bonding

force is 600 N, which is much higher than the plateau with 36 N in this experiment [107].

4.2.1.3 Strain hardening

The third stage is called the strain hardening stage. As the tensile elongation continue, the tablets begin to interlock to resist deformation, at which point the curve follows a linear trend, rising from the plateau stage until reach the ultimate tensile strength (UTS). The hardening of all multi-material structure specimens began at around strain 1% and UTS increases significantly with increasing dovetail angle. The hardening range (until reached the UTS point) for multi-material structure with 0˚ and 1˚ dovetail specimens is around strain 2.2%, 3˚ dovetail specimens have hardening range of strain 3.3% and 5˚ dovetail specimens have a total hardening range of around strain 4.7%. Stress levels also increase with dovetail angle growth, when the dovetail of multi-material structures at larger angles, with UTS for 0° being 5.93 MPa and 12.19 MPa for 5˚, increasing of 2 times. This variation could be due to the interlocking effect, resulting in increased shear resistance leading to strain distribution across the short and long interfaces [75].

The multi-material structure with 9˚ dovetail specimen does not show the expected stress-strain response, with a hardening range of around strain 4.5% , which is same with the results of 5˚ dovetail specimen, but the ultimate tensile strength is only 6.51 MPa, which is even lower than the 1˚ dovetail specimen (still higher than the non-interlocking 0˚ angle specimen). The 9˚ dovetail specimen was subjected to a comparison experiment with eight re-prints, with new printing parameters being adjusted on the last two re-prints, such as increasing the multiplier of PLA or install the new printing nozzle to avoid potential nozzle ware being a possible cause. PLA & TPU 9˚ dovetail specimens with the new print parameters are shown in the Figure 4.6, but the tensile results were still similar and showed lower UTS than the 5˚ dovetail specimen. Assuming this is due to a printing defect in the printer. Another reason is that 5˚ dovetail is the best choice for multi-material structure and 9˚ dovetail has lower

performance due to mechanical reasons. A computer simulation test should be considered for future work.

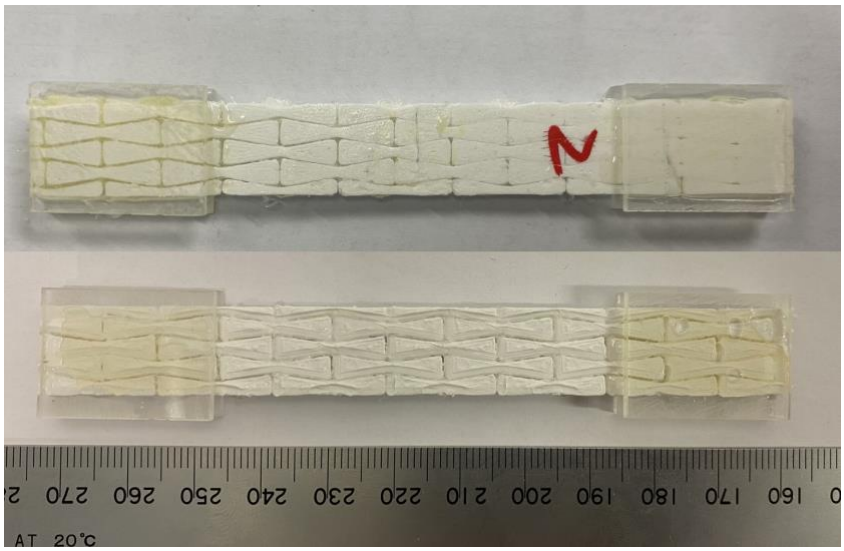

Figure 4.6. New (above)/ original (below) printing parameter for multi-material structure 9˚ dovetail specimen.

4.2.1.3.1 Secondary strain hardening

The stress drop after UTS is caused by the start short interface broken and the reduction of the overlap area or transverse compressive stress area, leading to a drop in stress levels during subsequent loading. Shear deformation along the long interface of the tablet then dominates. Before entering the long interface broken stage, the stress-strain curve for the multi-material structure with larger dovetail angle (5˚ and 9˚) specimens has a small rise, indicating secondary hardening. This is due to the larger angle of the tablets beginning to interlock to resist tension, which leads to high shear deformation during sliding [2], resulting in the non-linear deformation.

The secondary hardening strength of the multi-material structure with dovetail 5˚ specimen is approximately 4.9 MPa, which is similar with the first hardening capacity of the non-interlocking, multi-material structure with dovetail 0˚. The presence of this significant secondary hardening due to the dovetail angle is interesting and effectively

improves the energy absorption performance of the structure, it has not been found in other studies of nacre-like, multi-material dovetail structures [75, 95].

4.2.1.4 Long interface broken

As the tension progressed, the tablets began to be gradually pulled out and localised shear damage occurred along the long interface of the tensile specimen. Figure 4.7 shows the shear diagram and force model for the long interface between the non-interlocked structure and the interlocked structure fracture section respectively. In tension, only parallel lateral shear effects occur in the non-interlocked structure, while the shear effects in the interlocked structure become greater due to the interlocking of the tablets [87]. At this point the cohesion between TPU and PLA at the long interface will not match the pull-out force and slowly fail, as shown by a small drop trend in the stress-strain curve. Multi-material structure with dovetail angle 0˚ and 1˚ long interface failures are both at around strain 11%, while dovetail angle with 3˚, 5˚ and 9˚ specimens are at around strain 17%. This corresponds to a large dovetail interlock structure will bear greater shear to resist tablet pull-out.

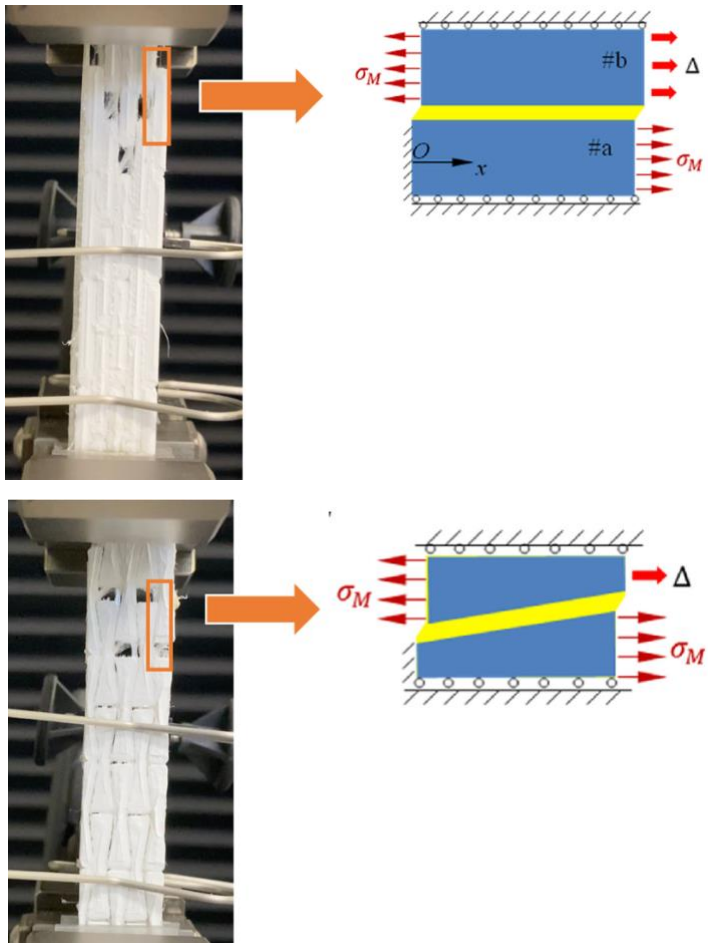

Figure 4.7. The image and stress model multi-material structure with 0˚ and 9˚ dovetail during tablets pull-out, where blue color is tablets, yellow color is filler [88]. Reprinted with permission from Elsevier.

4.2.1.5 Flexible filler material elongation

After the tablet is completely pulled out, the remaining mechanical response comes from the elongation of the TPU mainly at the long interface where the structural fracture occurs. In the experiment, it was also found that this stage may contain a portion of short interface rupture and oblique long interface TPU fracture as shown in the Figure 4.8, multi-material structure with dovetail 9˚ specimen underwent both long and short interface broken during tensile test and the red cycle with dash line in Figure 4.9 shows the oblique TPU strands from long interface. This occurred because the overall structure of the layer multi-material structures would cause the entire tablets to gradually ‘lock up’ during loading, extending the damage to a large number of tablets,

thus causing the short interface at the non-ruptured interface to break along with the long interface at the ruptured interface.

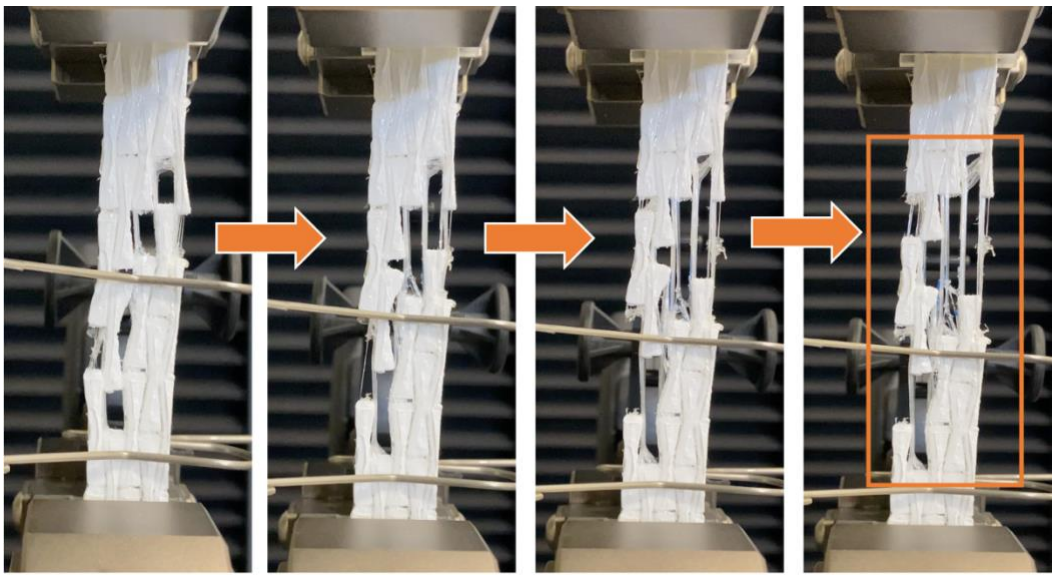

Figure 4.8. After tablet fully pulled-out, long and short interface broken of multi-material structure with 9˚ dovetail during TPU elongation section.

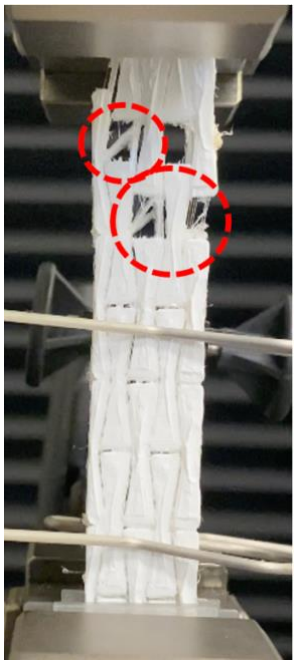

Figure 4.9. Oblique TPU strands at long interface of multi-material structure with 9˚ dovetail specimen during tensile test.

Several samples also selected for the experiment make strain to complete fracture, it takes 40 minutes due to high elongation at break of TPU. Long periods of TPU tensile process were also found in the experiments by Ko et al. [107]. Figure 4.10 displays the

gradual fracture of the filaments of the TPU, which caused low stress fluctuations in the stress-strain curve showing in Figure 4.11 at strain between 100% and 400%.

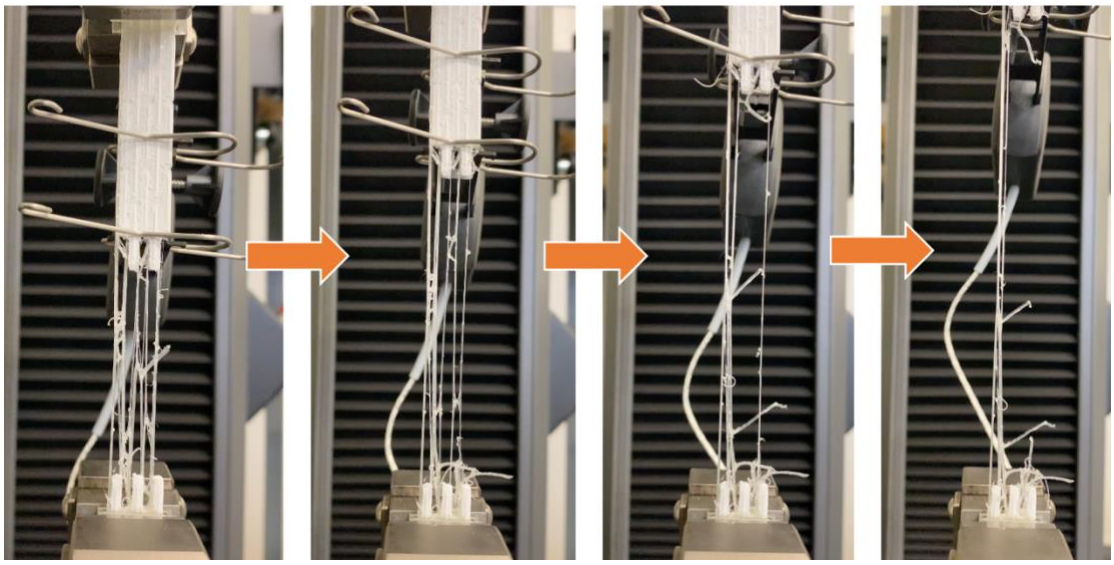

Figure 4.10. The gradual fracture process of TPU filament of multi-material structure with 5˚ dovetail.

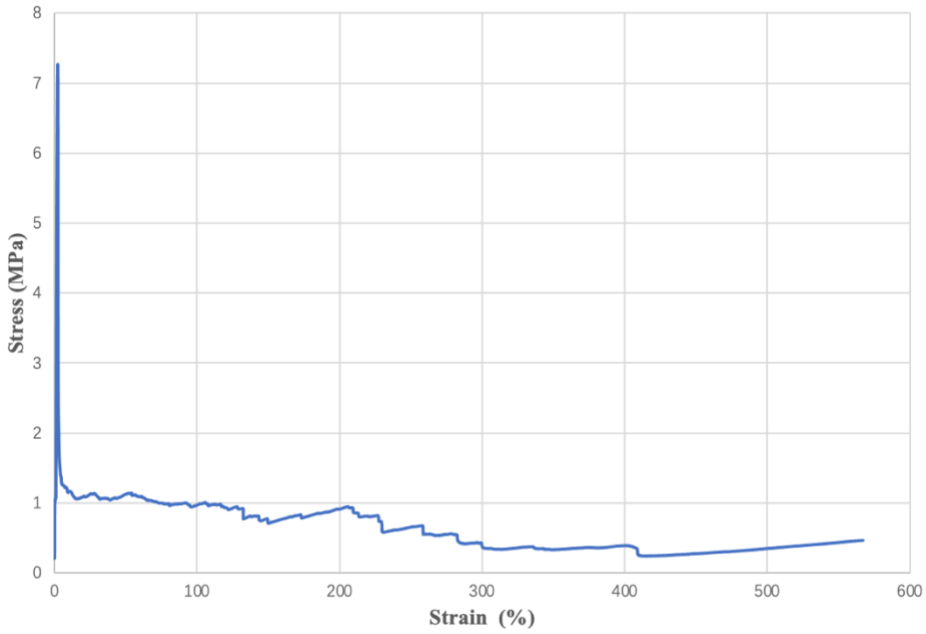

Figure 4.11. Stress-strain relationship of multi-material structure with 5˚ dovetail specimen for elongation to break.

4.2.2 Tensile test failure mode

Failure modes of nacre-like, multi-material structures can be broadly classified as tablet pull-out and tablet break fracture [75]. Both failure modes were observed in this

experiment. Tablet break was commonly happening in the middle narrow section of tablets, it will occur when the maximum stress exceeded the tablet strength. When the maximum stress does not exceed the strength of the tablet, the tablet pull-out will happen. Tablet pull-out is the ideal failure mode to improve the structural toughness of the nacre-like multi-material layer structure.

The combination of tablet pull-out and tablet break was proposed to create maximum stress and energy absorption properties [75], corresponding to increase the area under the stress-strain curve for the maximum stress the material can withstand before failure. The comparison tensile results and photographs of two failure mode were shown in Figure 4.12 and Figure 4.13. The tensile strength of the combination of the two fracture modes is 5 MPa higher than that of tablet pull-out alone.

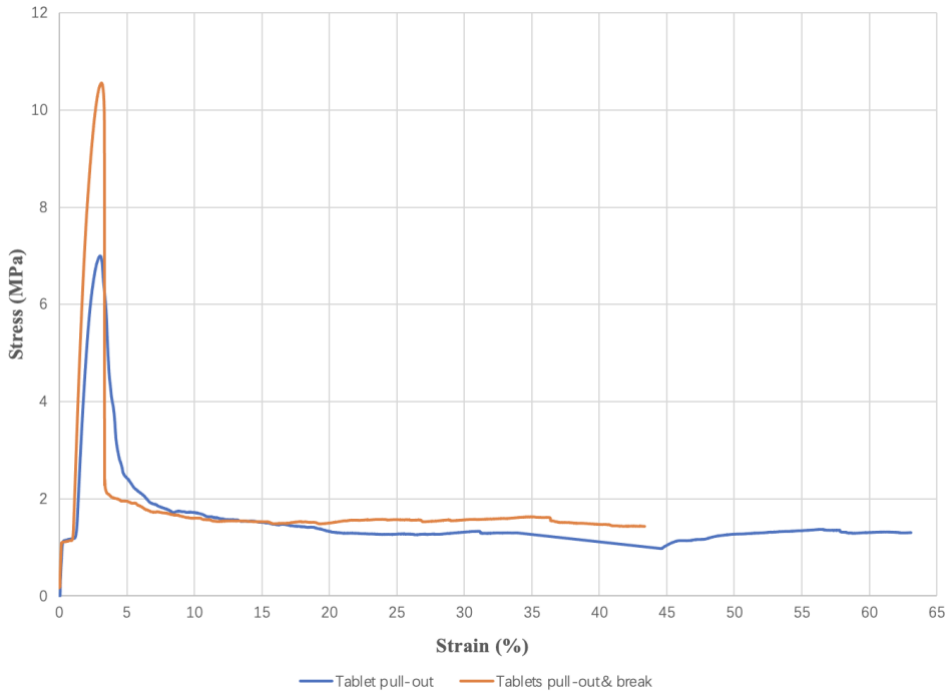

Figure 4.12. Comparison tensile curve of tablet pull-out and tablet pull-out & break from multi-material structure with 3˚ dovetail.

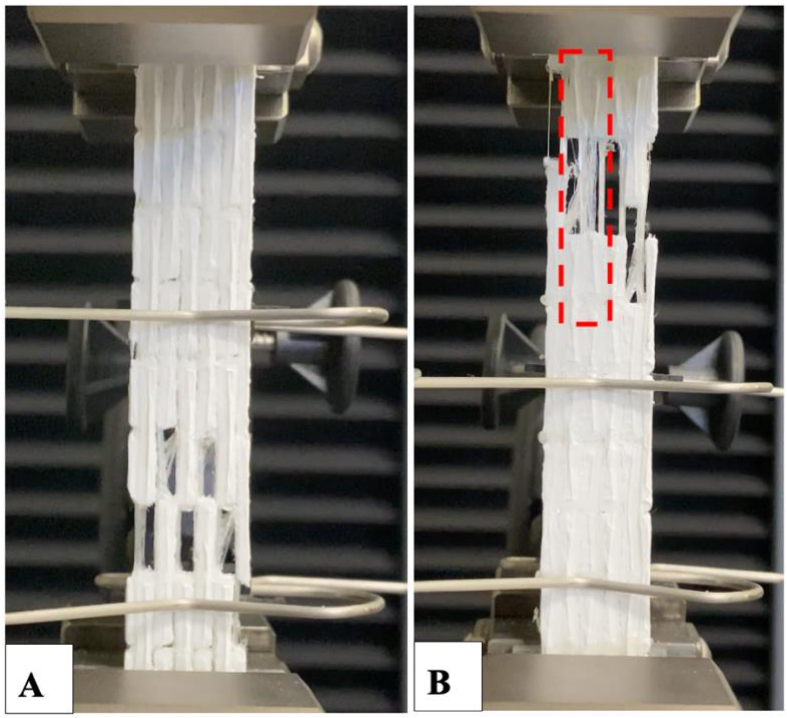

Figure 4.13. (A) Photographs for multi-material structure with 1˚ dovetail showing tablet pull-out. (B) Multi-material structure with 5˚ dovetail showing tablets break, as seen in red dash line square.

4.2.2.1 Tablet pull-out mode

Reza et al. [108] proposed that there are two types of tablets pull-out fracture in interlocking multi-material structures during deformation, namely columnar and non-columnar fracture, as shown in Figure 4.14. Both fracture modes were indeed observed in the tensile tests. The multi-material structures with small dovetail angles 0˚, 1˚ and 3˚ specimens were all appears columnar fractures with only a single non-columnar fracture observed. As the dovetail angle of multi-material structures increased, the occurrence of non-columnar fractures increased, all specimens of multi-material structure with 9˚ dovetail were non-columnar fractures or a combination of both, as shown in Figure 4.15.

Ghimire et al. [95] suggest that an increase in the number of non-columnar fractures will allow the non-linear deformation mechanism to occurrence, increasing the strength

of the overall structure and absorbing more energy, but this was not found in the results of this experiment.

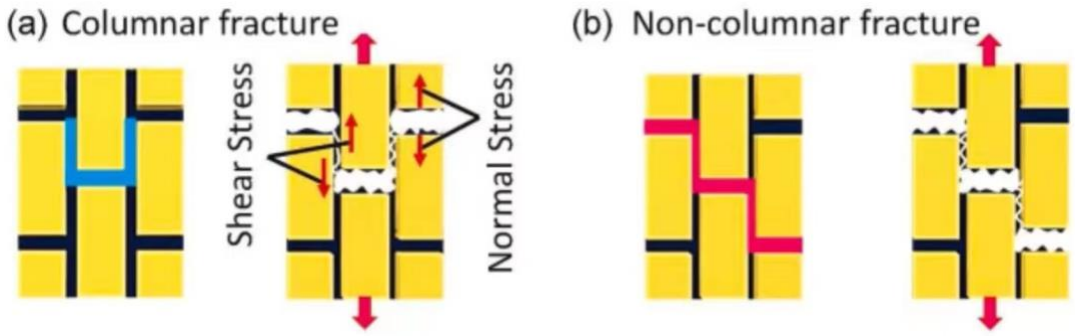

Figure 4.14. Sketch of columnar, and non-columnar fracture, where the yellow color is tablets, blue and red color line is the fracture type [95]. Reprinted with permission from Elsevier.

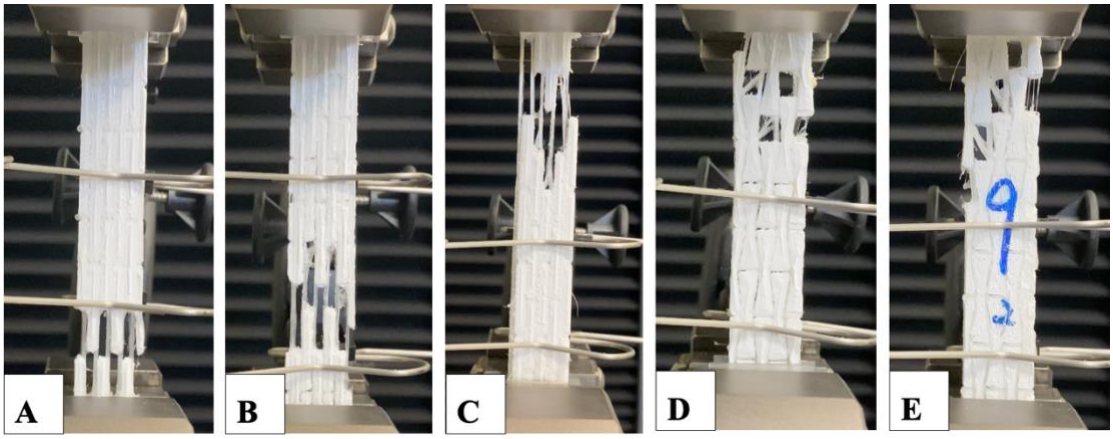

Figure 4.15. (A), (B) Columnar fractures in multi-material structure with 1° dovetail specimen. (C) Non-columnar fractures in multi-material structure with 9° dovetail specimen. (D), (E) The combination of two tablets pull-out fracture types in 9° dovetail specimen.

4.2.2.2 Tablet pull-out & break mode

In this experiment, tablet break usually accompanied tablet pull-out, tablet break in whole cross-section was only found in specimens printed under the new printing parameters as shown in Figure 4.16, which may be due to excessive joint between TPU and PLA filament, allowing the interface to withstand much greater forces than the strength of the tablet.

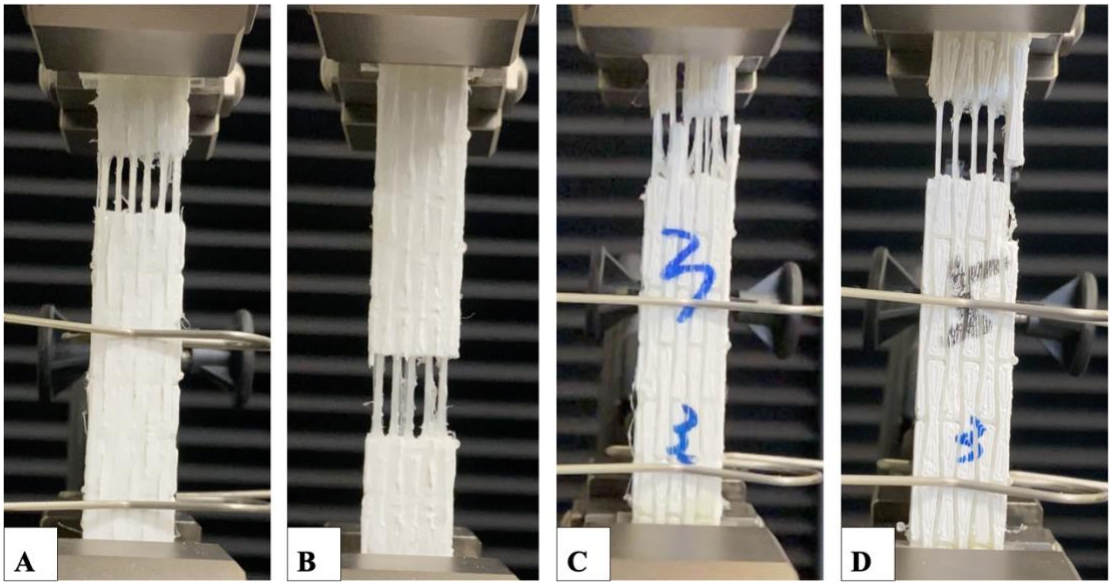

Figure 4.16. (A), (B) All tablets break for multi-material structure with 3˚ dovetail specimen under new printing parameters. (C), (D) Combination of tablets pull-out and break fracture mode on multi-material structure with 3˚ and 9˚ dovetail.

4.3 Poisson's ratio

The width of the multi-material structure was observed to expand under large dovetail angle, showing the effect of a negative Poisson's ratio. Figure 4.17 shows the width expansion response of the multi-material PLA & TPU with 9˚ dovetail specimen during the tensile test. The transverse strain of the specimen was measured and calculated in the same way as the longitudinal strain, at the section of the structure where fracture occurred.

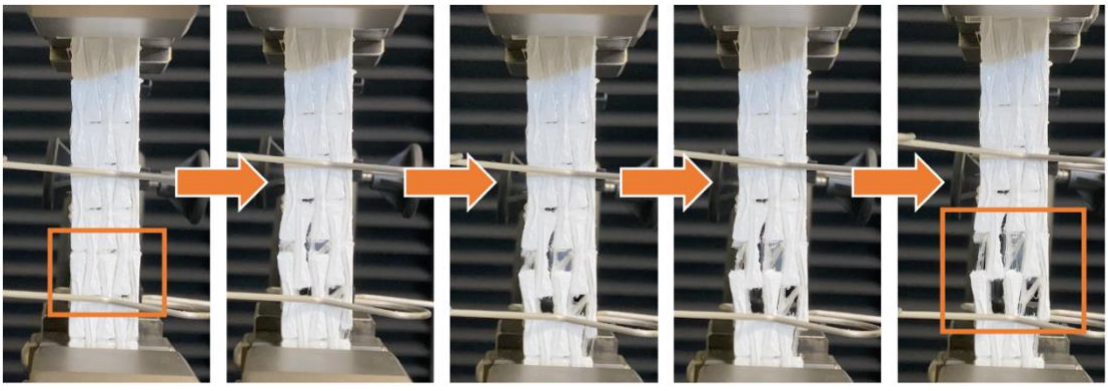

Figure 4.17. Expand width of multi-material PLA & TPU structure with 9˚ dovetail during tensile process.

The calculation results for PLA & TPU 5˚ and 9˚ dovetail specimens are shown in Figure 4.18. The Poisson's ratio values are negative, with larger values for the 9˚ specimens, confirming the presence of a negative Poisson's ratio effect in the larger dovetail structure during tablet pull-out process. There was no observed shrinkage due to the Poisson effect in the tablets in the experiments because tablet sliding was the dominant mode deformation in PLA & TPU dovetail specimen. When the tablets slide against each other, there may be some lateral expansion in the transverse direction counteract the normal positive Poisson's effect [2].

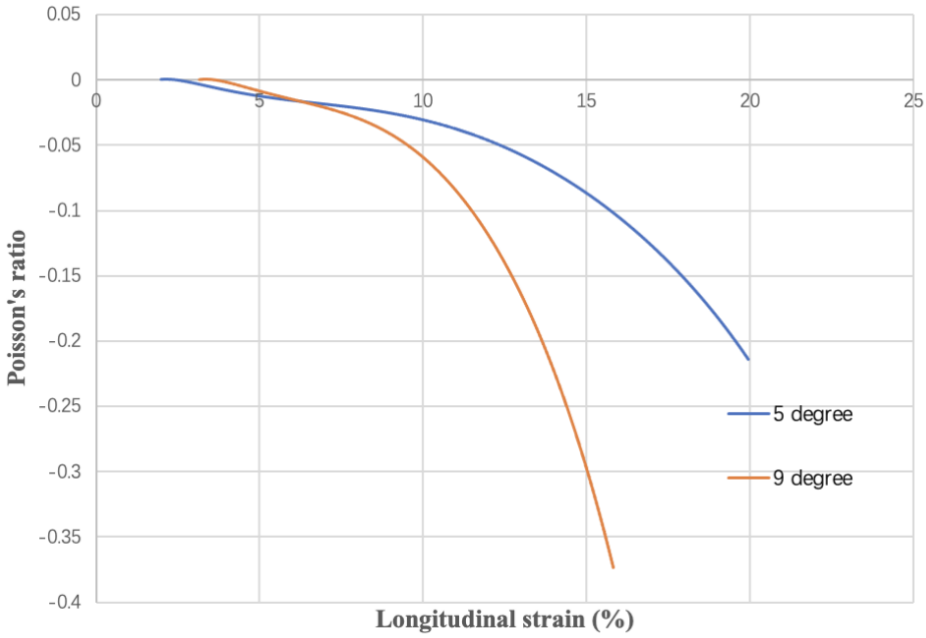

Figure 4.18. Relationship between Poisson's ratio and longitudinal strain of multi-material structure with 5˚ and 9˚ dovetail specimen.

Multi-material structure specimens with dovetail PLA & PLA with 0˚ and 5˚ dovetail and unidirectional pure PLA specimens were used as a comparison to discuss the effect of soft fillers on tablet sliding. The experimental results are shown in Figure 4.2. The failure mode is shown in Figure 4.19. Both specimens exhibited brittle material fracture characteristics and did not show any observable width extension during the test. It can be determined that brittle filler cannot withstand large deformations (may fail at small strains) [2]. The presence of a soft filler allows the interface to deform and maintain cohesion between the tablets at larger strain, which is important for the tablets to slide

and achieve large tensile strength. Experiments by Smith et al. [109] proved that the soft organic interface has the ability of large extension through tablet arrangement.

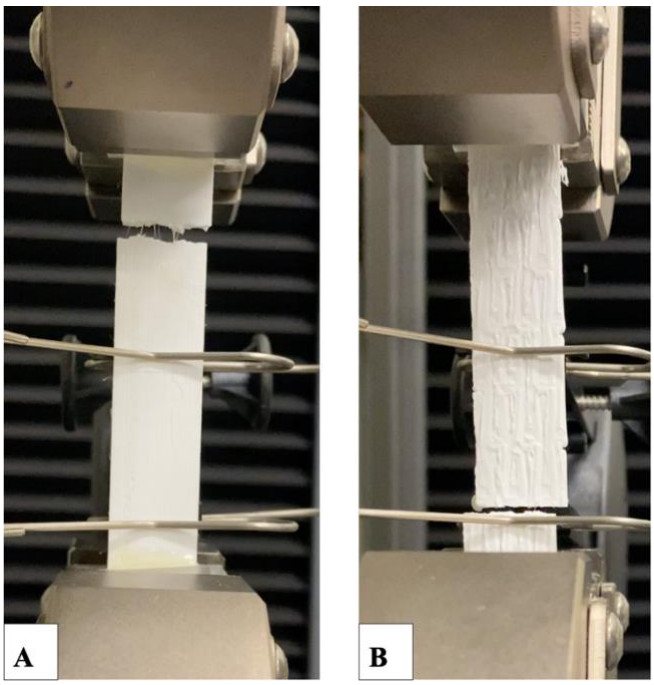

Figure 4.19. Failure mode of unidirectional pure PLA specimen and dovetail PLA & PLA structure with 5˚ dovetail specimen.

4.4 Fracture toughness results

Multi-material structures with 0°, 5° and 9° dovetail were selected for the fracture toughness testing and the force-displacement results are shown in Figure 4.20. The curve has approximately the same trend and are divided into three stages. As the specimen begins to be loaded, the tablet under the crack begins to rupture, causing the rise in force. After the tablets was broken, the crack continues and deflects along the nearest long interface, at which point the tablets interlocks to resist deformation, resulting in a slight increase in force level. In the final stage the interlocking effect fails and the cracking proceeds along the short interface or the rupture of the next tablet until the specimen is completely ruptured.

Lin et al. suggest that the crack extension along the long interfaces during fracture provides a damage tolerance feature for the structure as the stress level recovers after

the first failure event and has a significant effect on the overall toughness of interlocking structures due to the presence of soft material fillers [86].

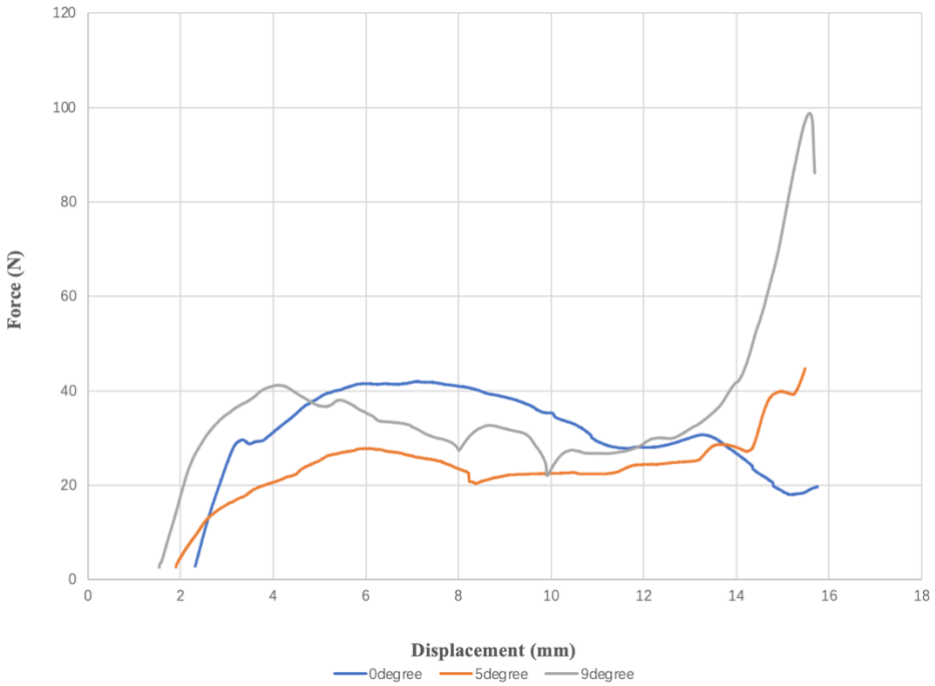

Figure 4.20. Relationship between force and displacement of selected 0˚, 5˚ and 9˚ dovetail specimens.

4.4.1 Fracture toughness test results calculation

The ASTM test standard requires a check of the ratio of P_Q and P_{max}. P_Q can be calculated by the force-displacement curve showing in Figure 4.21. The slope of the line AB can be obtained by plotting the line against the raw data set and fitting a polynomial metric with order 6. The slope of the line AB' can be obtained by selecting a linear data interval and the slope of the line AB' according to the 1.05*compliance line AB slope. These three line all pass through the x-axis, from which the curve formulae for both can be derived. The co-ordinate points of P_Q were found using MATLAB. Unfortunately, the P_{max}/P_Q values for tested multi-material structure with 0˚, 5˚ and 9˚ dovetail specimen all above 1.1, these was not invalid experiment results according to the ASTM standard.

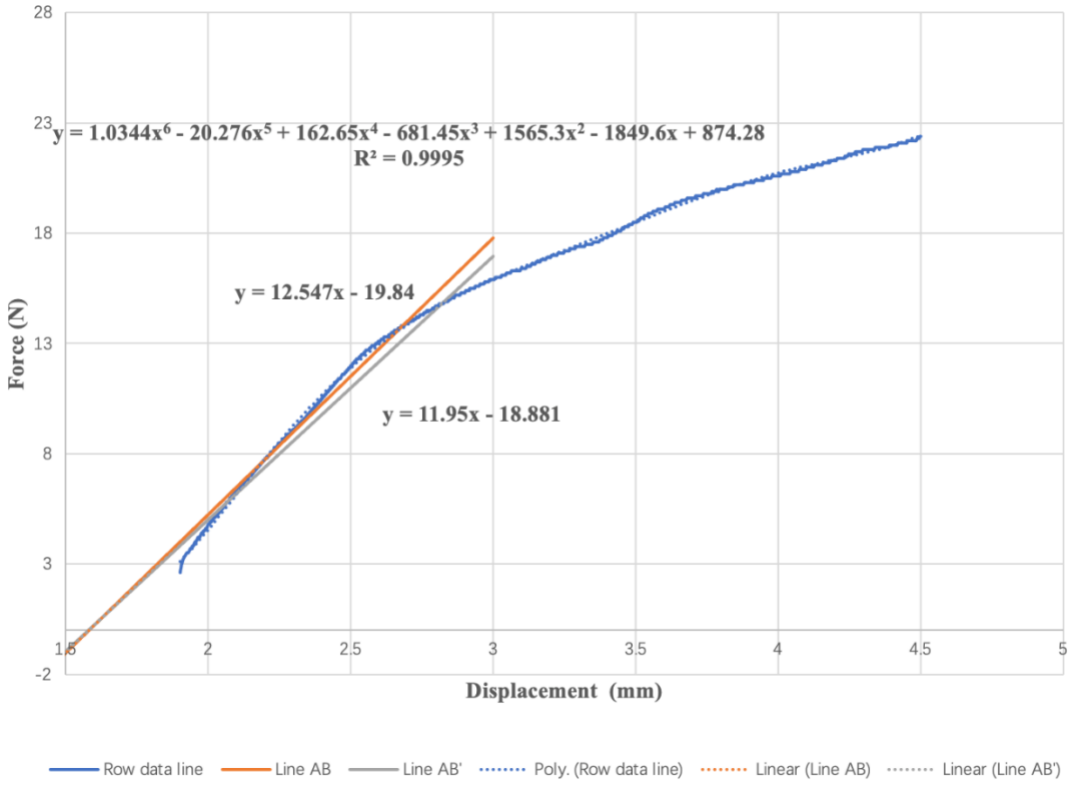

Figure 4.21. Force-displacement curve for 5˚ dovetail specimen showing row data, line AB and line AB'.

4.4.2 Fracture toughness failure mode

Figure 4.22 shows the fracture process of multi-material with 0˚ dovetail specimen. Cracks are expanding along the boundary of the tablet. The specimen size chosen for this experiment was too small, larger sizes were tested in other studies [55, 68, 110]. Crack development was observed in a direction perpendicular to the original crack, expanding only through the flexural filler patterns, leading to the eventual failure of the multi-material structure. Figure 4.23 illustrates the crack expansion path of other fracture toughness specimen study with multi-material structures, where the crack can be seen to move along the boundary of the tablet.

This pattern of crack extension is thought to be a characteristic toughness mechanism for a particular alignment, as the large difference stiffness between the tablet and filler material is conducive to the crack propagation through soft material in terms of energy.

The energy principle is applied to predict that the crack will choose the path with the least resistance, which is the most favorable energy path [110].

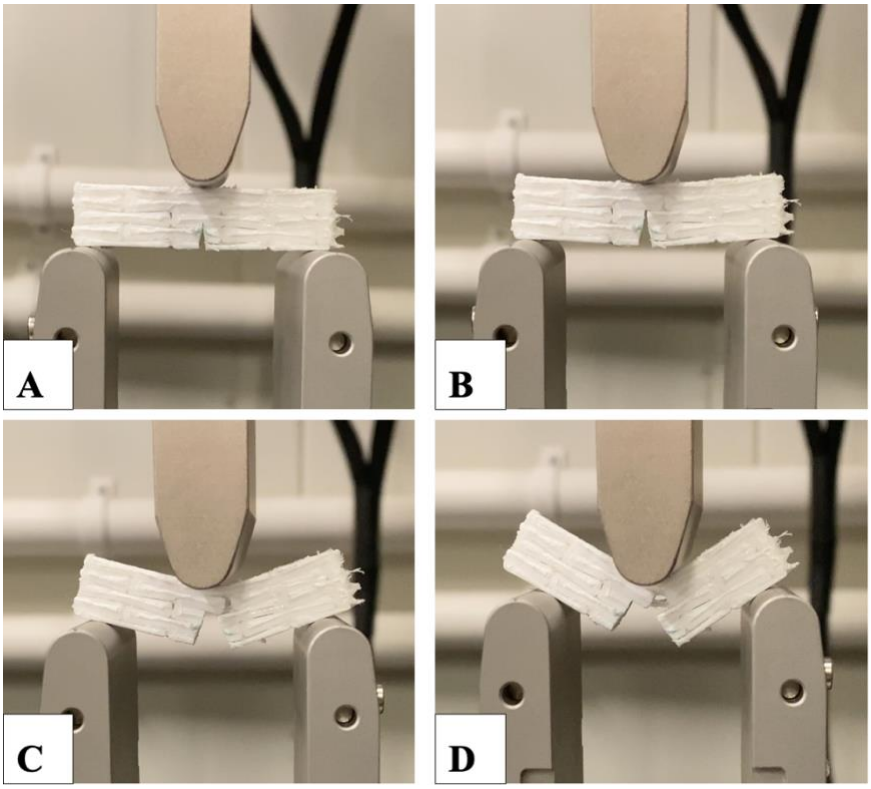

Figure 4.22. Fracture process of multi-material structure with 0˚ dovetail.

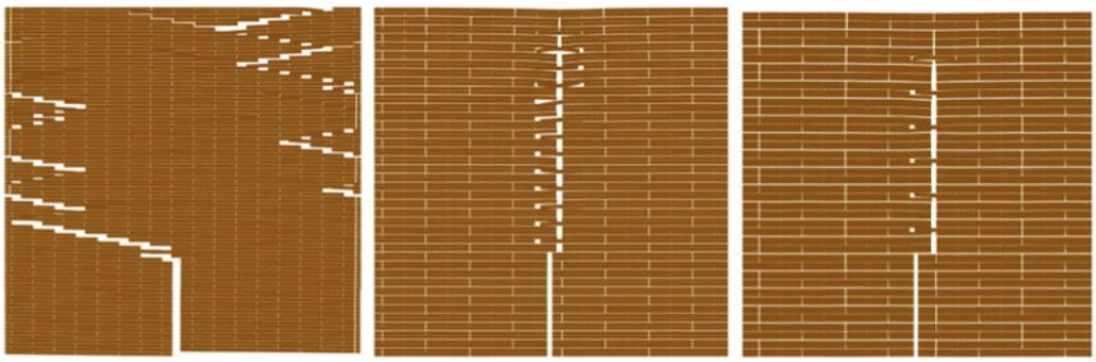

Figure 4.23. Crack propagation for 3D printed, nacre-like, multi-material structure with a pre-crack 30% the total length [68].

4.5 Cyclic tensile test results

The comparison stress-strain curve for 3D printed, multi-material structure with 0˚ and 5˚ dovetail specimen under tensile test and cyclic tensile test is shown in Figure 4.24 (A) and Figure 4.25 (A). And the cyclic tensile stress-strain curves of 0˚ and 5˚ dovetail

specimen for each cycle are also shown. The results for the 0˚ dovetail specimen only show three stages, Cycle 1, Cycle 2, Cycle 3 and Stage 6. The other cycles disappear presumably because the maximum stress did not reach 4 MPa in Cycle 3 and was skipped to the next cycle, however the 0˚ dovetail specimen also did not reach the strain range for Cycle 4 and Cycle 5, so the specimen went straight to the final step of uniaxial tensile test. For the results of 5˚ dovetail specimens, the change in the first three cycles was not significant, and there was a large change from Cycle 4 to 5, indicating mostly plastic deformation in the last two cycles.

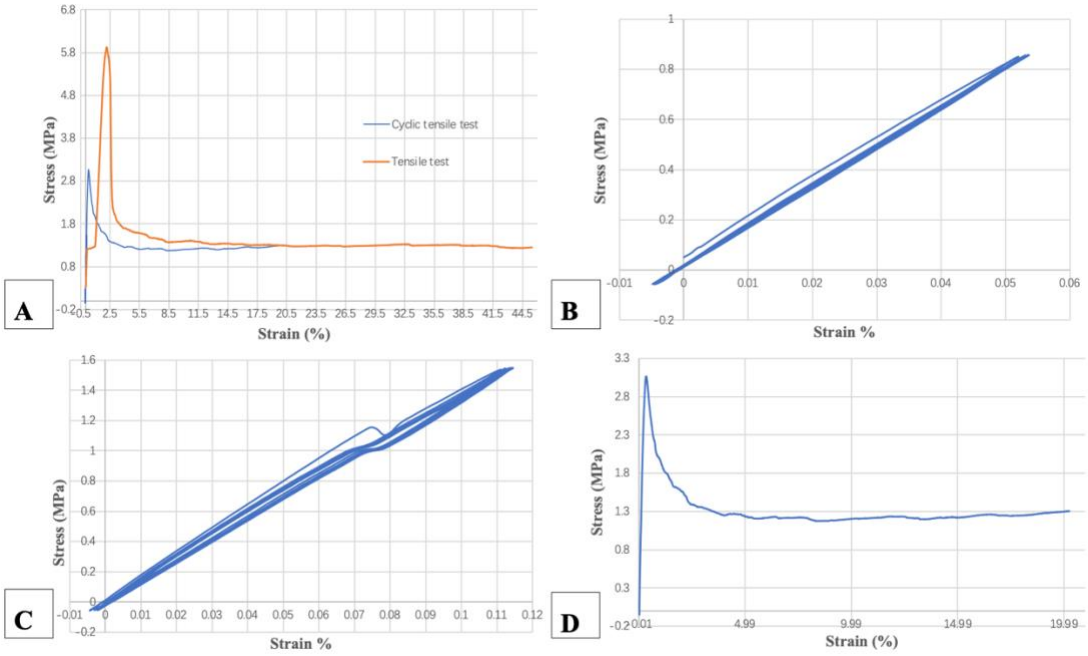

Figure 4.24. (A) Comparison results of multi-material structure with 0˚ dovetail under tensile test and cyclic tensile test. (B) Cyclic tensile stress-strain curve of 0˚ dovetail specimen for Cycle 1. (C) Stress-strain curve for Cycle 2. (D) Stress-strain curve for Cycle 3 and Stage 6.

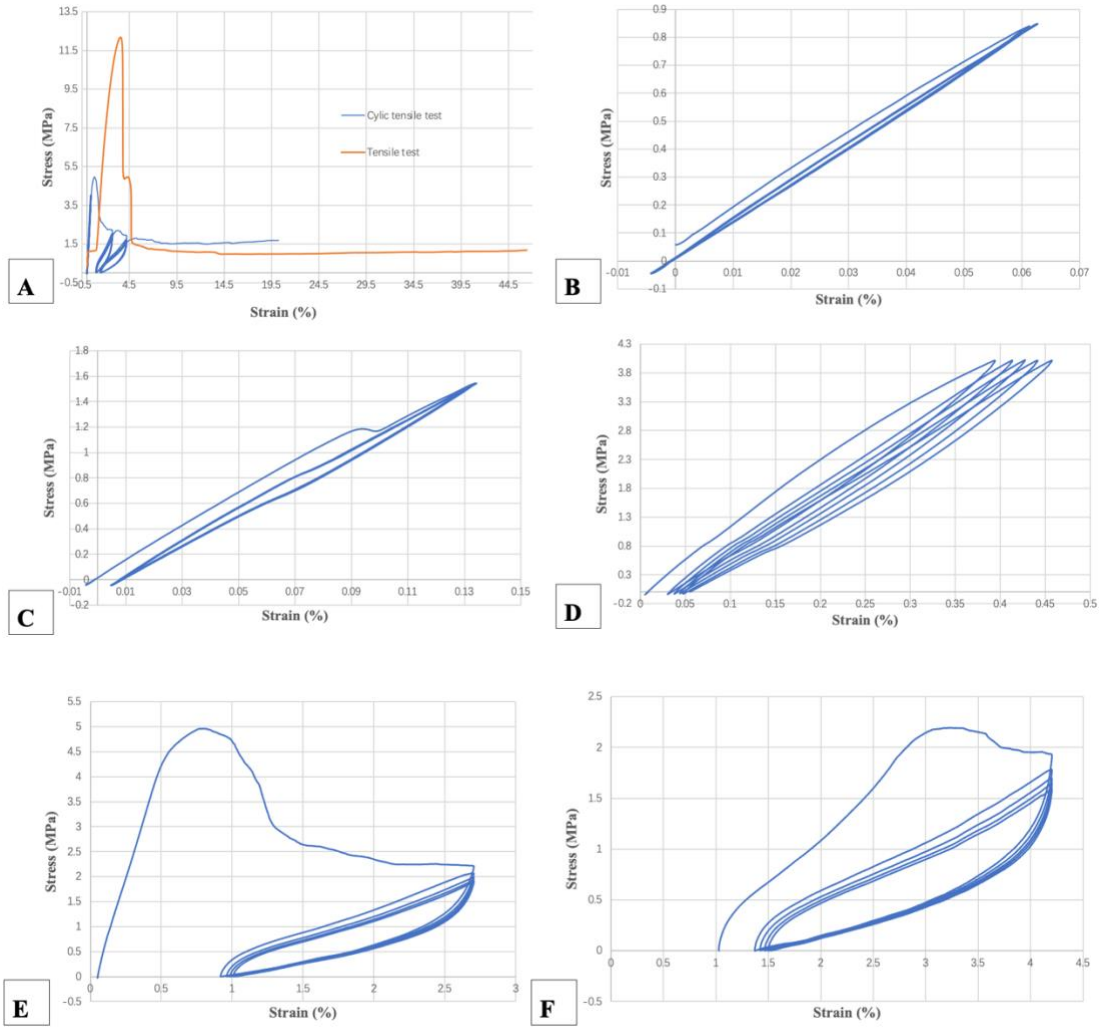

Figure 4.25. (A) Comparison results of multi-material structure with 5˚ dovetail under tensile test and cyclic tensile test. (B) Stress-strain curve of 5˚ dovetail specimen for Cycle 1. (C) Stress-strain curve for Cycle 2. (D) Stress-strain curve for Cycle 3. (E) Stress-strain curve for Cycle 4. (F) Stress-strain curve for Cycle 5.

4.5.1 Plateau region in cyclic tensile test

The results of multi-material structures with 0˚ and 5˚ dovetail cyclic tensile tests showed permanent changes in the repletion of the curve for Cycle 2 as shown in Figure 4.24 (C) and figure 4.25 (C), indicating the plastic deformation.

Although the results are not similar to the other studies, it is still assumed that that the occurrence of plateau is the yield of multi-material structure, and large tensile strain occurs at the short interface at the end of some of the tablets in the specimen (no evident

crack damage were seen in the recording), resulting in appearance of the plateau zone. The after loaded to 1MPa specimens were observed by microscopy and the short interfaces showed irrecoverable pores and gaps, as shown in Figure 4.26. Structures with plateau stage under force could be used as a protective material for applications, where the structure remains shape un-changed when subjected to damage below the yield stress.

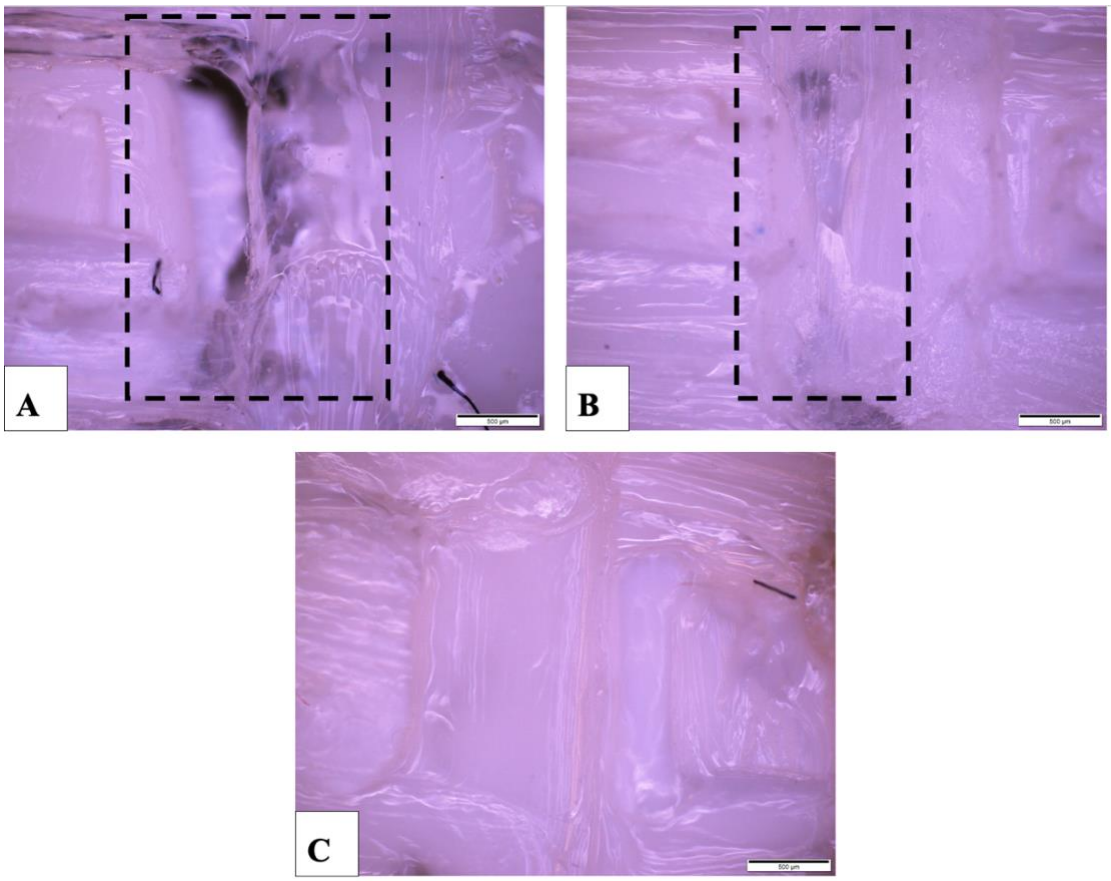

Figure 4.26. (A), (B) Pores and gaps (black dashes frame) in short interface of loaded multi-material 5˚ dovetail structure. (C) Preloaded short interface, in 500 μm.

4.5.2 Strain hardening in cyclic tensile test

Figure 4.27 shows the cyclic tensile test and fracture morphologies for multi-material structure with 5˚ dovetail specimen. Both Cycle 4 and Cycle 5 underwent substantial plastic deformation during the first loading. Inspection of the recordings shows that the short interface has fractured before the first loading starts. By the time the cyclic tensile curve reaches the peak point, the tablet is in the process of pulling out and the locking

of the dovetail angle with the shearing of the tablet provides a substantial rise in stress. The loading response of Cycle 5 is considered to be continuation of the Cycle 4, during which the tablet is repeatedly partially pulled out and the long interface between the tablet and the filler is broken.

Comparing the results of the two tests, Figure 4.27 (A) shows that Cycle 4 and Cycle 5 are occurring under the range of strain hardening stage and secondary strain hardening stage. It can be demonstrated that the maximum stress used to resist deformation when the multi-material structure under loaded comes from the shearing and rupture of the long interface between tablets and filler when the dovetail tablets are starting to pulled out.

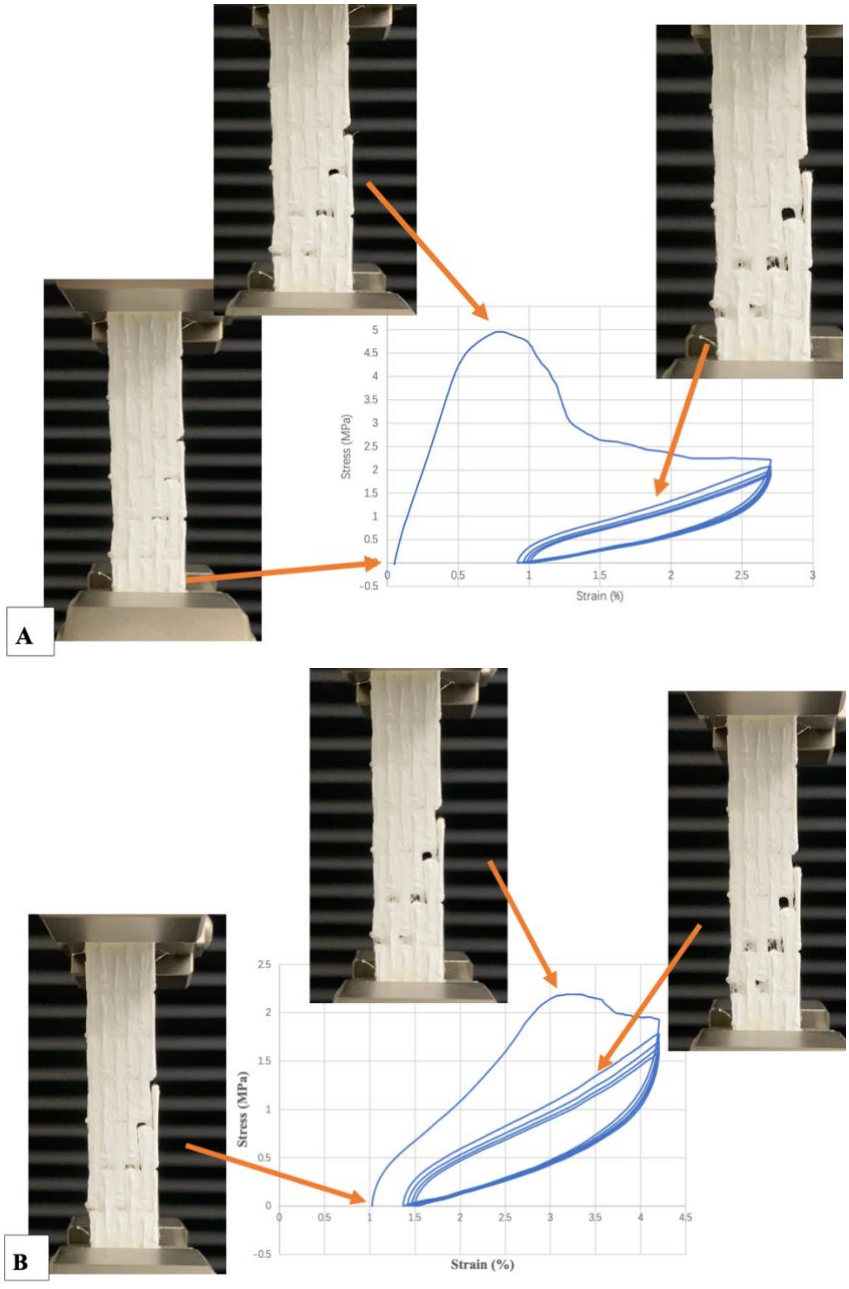

Figure 4.27. Fracture morphologies for 5˚ dovetail specimen during cyclic tensile test in (A) Cycle 4 and (B) Cycle 5.

4.6 Energy absorption and damage

It is important to understand the energy dissipation as multi-material structure is loaded to fracture, this can be expressed as energy absorption properties, corresponding to the toughness of structure. The energy absorption results of area under the stress-strain

curve before the UTS point and area under the whole curve for all specimens are shown in Figure 4.28.

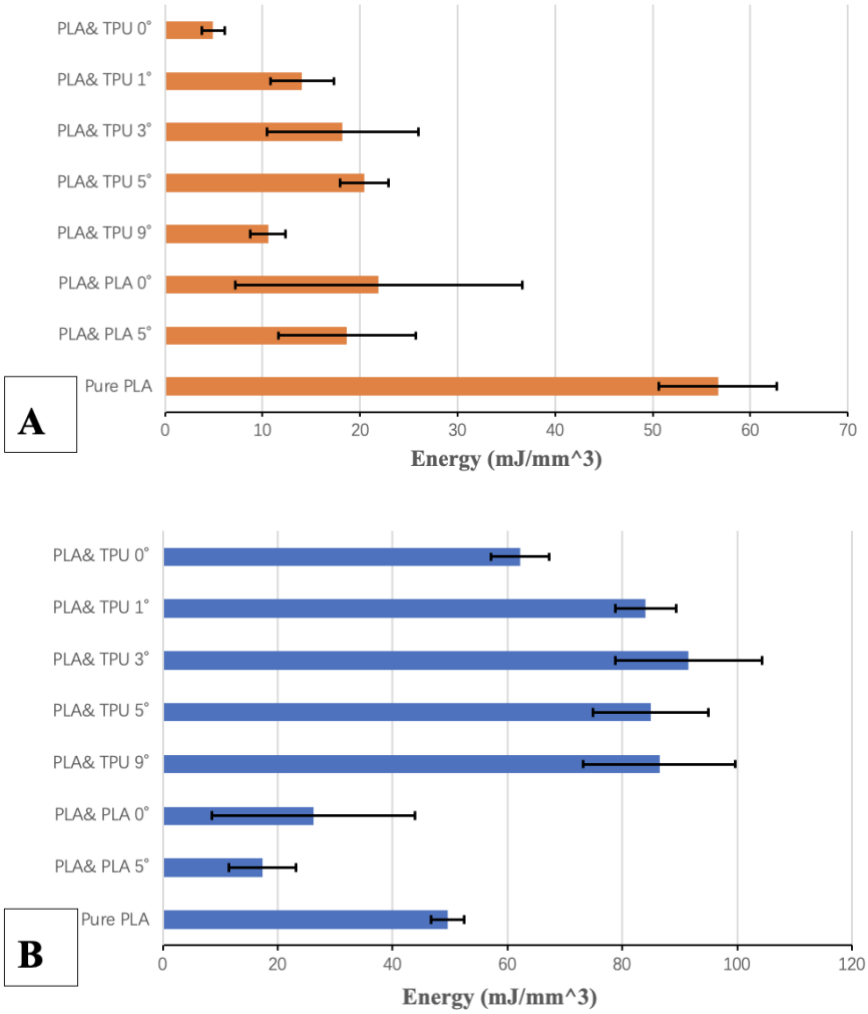

Figure 4.28. Energy absorption of multi-material structures (A) Area under curve before ultimate tensile strength. (B) Area under whole curve (end at elongation distance 20mm). Error bars are standard deviation.

The area under the curve before the appearance of UTS corresponds to the energy absorption properties during short interface broken and interlocking. The UTS of the multi-material PLA & TPU structure specimens increases with dovetail angle growth and the energy absorption values increase accordingly. Considering that the multi-material structure with 1˚ dovetail specimens does not show a yield plateau region, it is expected that the values will decrease slightly if yielding occurs, which is still consistent with this pattern.

Area under the whole curve include the same elongation displacement of the TPU after the tablet starts to be pulled out. Considering the higher volume percentage of TPU in the multi-material with 1˚ and 3˚ dovetail structures, it can resist more forces during tension, the stress level is higher in the long interface broken and TPU elongation region, which has a higher energy absorption value. In the tablet pull-out mode, the structure with higher filler volume will have higher energy absorption properties due to the high ductility of the filler [75]. Compared with the energy absorption performance of 3D printed, nacre-like structure by Ghimire et al. [95], the values are approximately twice high. For both dovetail PLA & PLA and unidirectional pure PLA specimens, the energy absorption performance in this region was much lower than that of multi-material PLA & TPU specimens, even lower than that of 0˚ dovetail specimens. It can be concluded that the addition of soft filler TPU can effectively increase the energy absorption performance of the structure, corresponding to the toughness of the structure.

The calculated damage resistance values for each cycle of the cyclic tensile test are shown in Figure 4.23. This result is calculated from the hysteresis of the load-unload curve. Using the traditional concept of continuum damage mechanics, damage is usually defined as a deterioration of the elastic modulus, which was found to occur in constant-amplitude tests [111, 112].

$$D = 1 - \frac{E_D}{E_0}$$

where E_D is the residual modulus of the damaged material and E_0 is the modulus of the undamaged material.

For the multi-material structure with 5˚ dovetail specimen, the first three cycles are mainly elastic deformation, the damage resistance level is very low. The last two cycles correspond to the region where the hardening mechanism occurs, showing a large energy dissipation. When damage resistance values are close to 1, large irrecoverable damage has occurred with the structure losing most of its stiffness. Elastic strain occurs

mainly in the first loading cycle. After the first loading, the values gradually decrease to a stable level as the number of cycles loaded. After this time, the energy loss due to damage may be mainly related to the long interface broken between the tablets and shear energy dissipation.

The multi-material with 0˚ dovetail structure demonstrates a low level of damage for Cycle 1 and Cycle 2, though failed completely at Cycle 3. It can be determined that the dovetail interlocking structure design prevents shear deformation and pull-out at the long interface and can absorb energy during the hardening stage more effectively than the non-interlocking design.

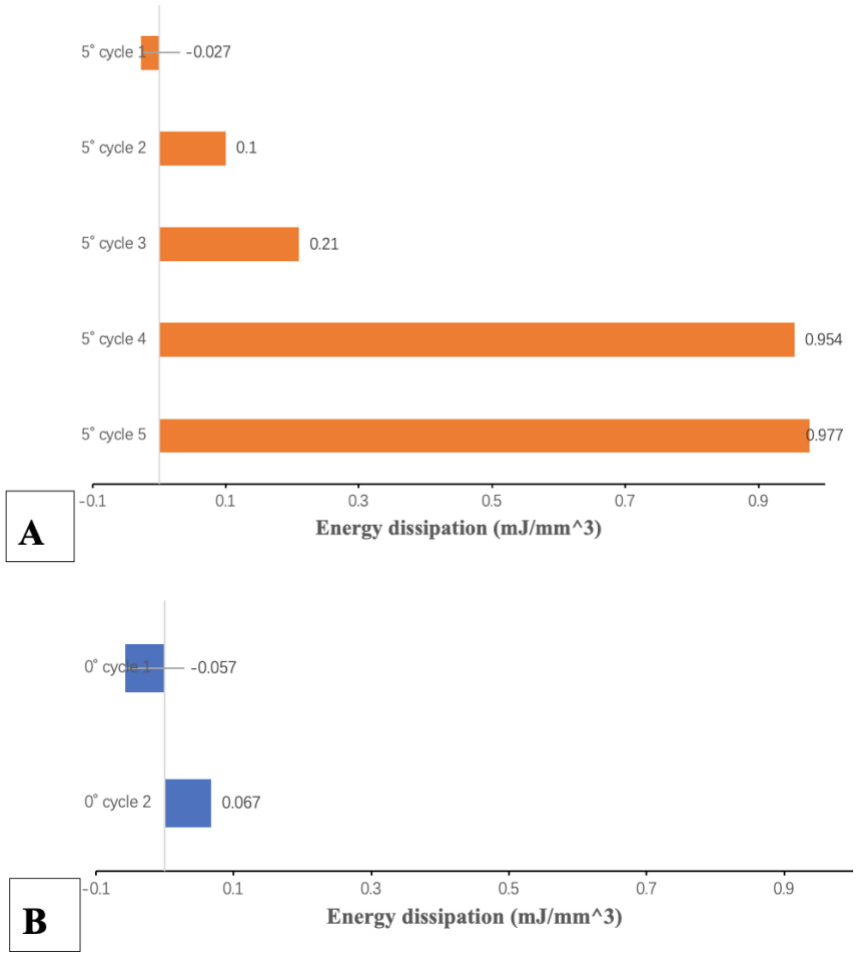

Figure 4.29. Damage for each cycle of multi-material structure under cyclic tensile test with (A) 5˚ dovetail and (B) 0˚ dovetail.

4.7 Summary

By comparing the tensile curves of pure PLA, dovetail PLA & PLA and multi-material PLA & TPU with dovetail angle specimens, it was determined that the presence of TPU (soft filler) can make the structure mechanical behavior complex, which exhibits multiple stages in stress-strain curve. The UTS value can be improved by adjusting the dovetail angle of the tablet, but the choice of the soft filler material is important. In the absence of the soft TPU filler situation, the stress-strain response of the dovetail PLA & PLA 0˚ and 5˚ dovetail specimen did not show differ significantly and behaved as a brittle material, same as the case of pure PLA specimen. The Young's modulus values of the multi-material PLA & TPU structures did not show a significantly increase with the dovetail angle growth. Therefore, it is not observed that increasing dovetail angle can improve the stiffness of multi-material, dovetail structures. The UTS and modulus of the multi-material PLA & TPU structure are not as high as those of pure PLA and PLA & PLA specimen, but energy absorption performance is improved by soft TPU filler and dovetail angles.

The cyclic tensile test has determined that the multi-material PLA & TPU structure plateau stage is yielding mechanism. The structure with the yield plateau stage can be used as a protective material in applications, where the structure remains shape unchanged after loaded when subjected to a force below the yield plateau stress. However, the fracture of the PLA tablet was observed in the multi-material PLA & TPU tensile test. In order to avoid this situation to maximize the sliding of the tablet, the size of the tablet (increasing the width of the central narrow section of the tablet) or the use of a harder tablet material should be considered. The cyclic tensile tests also determined that the resistance to deformation of the multi-material PLA & TPU structure when subjected to load is mainly due to interlocking and shearing between the dovetailed tablets.

In summary, the experimental results demonstrate that the addition of soft TPU filler reduces the overall stiffness of the structure, but effectively improves the toughness. With the addition of soft TPU filler, the hardness of the multi-material structure can be effectively improved by increasing the dovetail angle of the tablet. However, the optimal angle of the dovetail of the tablet has not yet been fully demonstrated in this thesis.

Chapter 5

Conclusion

Inspired by the high stiffness and toughness of the natural nacre structure, this thesis used 3D printing technology to prepare bio-inspired, multi-material structures and tested the relationship between dovetail angle and tensile behavior, failure modes and fracture toughness under the combination of soft and stiff materials by combining tensile test, cyclic tensile test and fracture toughness test.

In the experiments, multi-material structure tensile specimens with different dovetail angles, cyclic tensile specimens and crack-containing toughness specimens were prepared using an FDM-type 3D printer, based on the layer structure of the nacre. The tensile tests were carried out to investigate in detail the deformation of the tensile specimens during the multi-stages such as short interface failure, tablet interlocking, tablet pull-out and break, long interface failure and soft filler elongation, as well as the energy absorption in the strain hardening region.

The experimental results show that the presence of soft TPU filler can make the tensile stress-strain curves exhibit multiple stages. The 0˚ and 5˚ of dovetail PLA & PLA specimen without soft TPU filler exhibited brittle material behavior under tensile testing, same as the unidirectional pure PLA specimens. Two failure mechanism modes were observed in the tensile test of multi-material PLA & TPU dovetail structure: tablet pull-out and tablet break. The combination of tablet break and pull-out mode can lead a higher tensile strength than tablet pull-out. Interestingly, in the tablet pull-out mode, transverse expansion was observed in the 5˚ and 9˚ dovetail structure during tension, with negative Poisson's ratio values obtained.

It was observed that the multi-material dovetail PLA & TPU structure had a distinct plateau stage during tensile test, and cyclic tensile test identified the generation of this

stage as the yield point, occurred at the short interface between PLA and TPU. The plateau stage was not reported in previous studies of nacre-like, multi-material structures. Cyclic tensile test also determined that the forces resisting deformation in the multi-material PLA & TPU structure mainly from the interlocking and shear between the dovetail tablets. Large dovetail angle tablets provide greater shear for the interlocking mechanism of tablet sliding, allowing more plastic deformation and absorbing more energy. In fracture toughness test, crack extension behavior was observed in fracture toughness specimens even though the experimental data proved to be invalid according to ASTM standard.

The multi-material PLA&TPU structure with 5˚ dovetail exhibited the highest ultimate tensile strength of 11.46 MPa and Young's modulus of 495.96 MPa, and the ultimate tensile strength increased with the dovetail angle increase until 5˚ but declined for the 9˚ dovetail specimen. The 0˚ dovetail specimen only had 5.6 MPa in tensile strength. Although the ultimate tensile strength and Young's modulus for dovetail PLA & TPU both less than the unidirectional pure PLA (ultimate tensile strength of 47.16 MPa, modulus of 2711.71 MPa) and 5˚ dovetail PLA&PLA structures (ultimate tensile strength of 27.73 MPa, modulus of 2712.42 MPa), but the energy absorption performance results far exceeded the indirection pure PLA specimens. This demonstrates that the combination of stiff and soft materials reduces the overall stiffness of the structure but can effectively improve the toughness. The ultimate tensile strength of the multi-material structures can be effectively improved by increasing the dovetail angle of the tablets with the incorporation of stiff and soft tablets and filler materials. But the large increase in stiffness with dovetail angle was not observed in the experiments. Experimenting with different materials and computer simulation tests should be considered in future work.

These observations in this thesis suggest that the design of 3D printed, bio-inspired, multi-material structures and the combination of effective materials can optimize the

mechanical behavior of the overall structure and improve its mechanical properties, could be an effective way to explore high-performance materials in the future.

Chapter 6

Recommendations

The results and observations of this project provide a basis for further research into the toughening mechanisms of 3D printed, nacre-like, multi-material structures. The following are some suggestions for future work in this area:

- Investigate the effect on mechanical properties at different tablet overlap ratio.
- Investigate the effect of different sizes of tablets on tensile properties.
- Investigate the shear transfer mechanism of stresses in nacre-like multi-material structures when subjected to forces.
- Establish the simulation experiment as a comparison to reduce the impact of print quality on the laboratory results.
- Build larger size tensile test specimens and toughness test specimens to complete the study of crack behaviour.
- Increase the width of the middle tablet or consider using a stronger tablet material to eliminate tablet fracture during tensile.
- Optimize the design of the tablet pattern to find the configuration that dissipates the most energy without breaking through the tablet sliding.

References

1. Fratzl, P., et al., *Structure and mechanical quality of the collagen–mineral nano-composite in bone*. Journal of materials chemistry, 2004. **14**(14): p. 2115-2123.
2. Barthelat, F., et al., *On the mechanics of mother-of-pearl: A key feature in the material hierarchical structure.* Journal of the mechanics and physics of solids, 2007. **55**(2): p. 306-337.
3. Currey, J.D., *Mechanical properties of mother of pearl in tension.* Proceedings of the Royal society of London. Series B. Biological sciences, 1977. **196**(1125): p. 443-463.
4. Jackson, A., J.F. Vincent, and R. Turner, *The mechanical design of nacre.* Proceedings of the Royal society of London. Series B. Biological sciences, 1988. **234**(1277): p. 415-440.
5. Meyers, M.A., et al., *Biological materials: structure and mechanical properties.* Progress in materials science, 2008. **53**(1): p. 1-206.
6. Mahindru, D., S. Priyanka Mahendru, and L. Tewari Ganj, *Review of rapid prototyping-technology for the future.* Global journal of computer science and technology, 2013.
7. Masood, S.H., *Advances in Fused Deposition Modeling*, in *Comprehensive Materials Processing*, S. Hashmi, et al., Editors. 2014, Elsevier: Oxford. p. 69-91.
8. Tolochko, N.K., et al., *Mechanisms of selective laser sintering and heat transfer in Ti powder*. Rapid prototyping journal, 2003.
9. Mao, H. and Z. Gu, *Development status and trend of polymer materials for biological 3D printing.* Development of materials in China, 2018. **37**(37).
10. Hirt, L., et al., *Additive Manufacturing of Metal Structures at the Micrometer Scale.* Advanced Materials, 2017. **29**(17): p. 1604211.
11. Clough, E.C., et al., *Elastomeric Microlattice Impact Attenuators.* Matter, 2019. **1**(6): p. 1519-1531.
12. Li, D., H. Lan, and B. Lu, *Micro-and nanoscale 3D printing.* Scientia Sinica Technologica, 2015. **45**(9): p. 919-940.
13. Chen, L., et al., *The research status and development trend of additive manufacturing technology*. The International Journal of Advanced Manufacturing Technology, 2017. **89**(9-12): p. 3651-3660.
14. Khosravani, M.R. and T. Reinicke, *On the environmental impacts of 3D printing technology*. Applied Materials Today, 2020. **20**: p. 100689.
15. Ngo, T.D., et al., *Additive manufacturing (3D printing): A review of materials, methods, applications and challenges.* Composites Part B: Engineering, 2018. **143**: p. 172-196.
16. Chan, H.K., et al., *The impact of 3D Printing Technology on the supply chain: Manufacturing and legal perspectives.* International Journal of Production Economics, 2018. **205**: p. 156-162.
17. Li, Y., et al., *A Review on Functionally Graded Materials and Structures via Additive Manufacturing: From Multi‐Scale Design to Versatile Functional Properties.* Advanced Materials Technologies, 2020. **5**(6): p. 1900981.
18. Kazmer, D., *Three-dimensional printing of plastics*, in *Applied Plastics Engineering Handbook*. 2017, Elsevier. p. 617-634.
19. Penumakala, P.K., J. Santo, and A. Thomas, *A critical review on the fused deposition modeling of thermoplastic polymer composites.* Composites Part B: Engineering, 2020. **201**: p. 108336.
20. Bing-he, L.H.-y.C.B.-r.L., *Analysis on Mechanical Property of 3D Printing Engineering Plastic*. Journal of Highway and Transportation Research and Development, 2017. **Vol.34**.

21. Wang, Y., et al., *Current Status and Prospects of Polymer Powder 3D Printing Technologies.* Materials, 2020. **13**(10): p. 2406.
22. Yao, T., et al., *A method to predict the ultimate tensile strength of 3D printing polylactic acid (PLA) materials with different printing orientations.* Composites Part B: Engineering, 2019. **163**: p. 393-402.
23. Popescu, D., et al., *FDM process parameters influence over the mechanical properties of polymer specimens: A review.* Polymer Testing, 2018. **69**: p. 157-166.
24. Hertle, S., M. Drexler, and D. Drummer, *Additive Manufacturing of Poly(propylene) by Means of Melt Extrusion.* Macromolecular Materials and Engineering, 2016. **301**(12): p. 1482-1493.
25. Chacón, J.M., et al., *Additive manufacturing of PLA structures using fused deposition modelling: Effect of process parameters on mechanical properties and their optimal selection.* Materials & Design, 2017. **124**: p. 143-157.
26. Gomez-Gras, G., et al., *Fatigue performance of fused filament fabrication PLA specimens.* Materials & Design, 2018. **140**: p. 278-285.
27. Tao Wu, R.N., Guangchun Wang, *Research progress of fused filament fabrication rapid prototyping technology.* China Academic Journal Electronic Publishing House, 2014. **Science & Technology Vision**: p. 94.
28. Zhong, W., et al., *Short fiber reinforced composites for fused deposition modeling.* Materials Science and Engineering: A, 2001. **301**(2): p. 125-130.
29. Da Silva, D., et al., *Biocompatibility, biodegradation and excretion of polylactic acid (PLA) in medical implants and theranostic systems.* Chemical Engineering Journal, 2018. **340**: p. 9-14.
30. Ohkita, T. and S.H. Lee, *Thermal degradation and biodegradability of poly (lactic acid)/corn starch biocomposites.* Journal of Applied Polymer Science, 2006. **100**(4): p. 3009-3017.
31. Torres, J., et al., *An approach for mechanical property optimization of fused deposition modeling with polylactic acid via design of experiments.* Rapid Prototyping Journal, 2016.
32. Nampoothiri, K.M., N.R. Nair, and R.P. John, *An overview of the recent developments in polylactide (PLA) research.* Bioresource technology, 2010. **101**(22): p. 8493-8501.
33. Kuznetsov, V.E., et al., *Strength of PLA components fabricated with fused deposition technology using a desktop 3D printer as a function of geometrical parameters of the process.* Polymers, 2018. **10**(3): p. 313.
34. Siakeng, R., et al., *Natural fiber reinforced polylactic acid composites: A review.* Polymer Composites, 2019. **40**(2): p. 446-463.
35. Cai, Y., et al., *Progress in the research and application of PLA materials in 3D printing.* Applied Chemicals, 2019(6): p. 47.
36. Tao, Z., et al., *Design and optimization of prosthetic foot by using polylactic acid 3D printing.* Journal of Mechanical Science and Technology, 2017. **31**(5): p. 2393-2398.
37. Elmrabet, N. and P. Siegkas, *Dimensional considerations on the mechanical properties of 3D printed polymer parts.* Polymer Testing, 2020. **90**: p. 106656.
38. Chen, Q., et al., *3D printing biocompatible polyurethane/poly (lactic acid)/graphene oxide nanocomposites: anisotropic properties.* ACS applied materials & interfaces, 2017. **9**(4): p. 4015-4023.
39. Tang, X. and X. Yan, *Acoustic energy absorption properties of fibrous materials: A review.* Composites Part A: Applied Science and Manufacturing, 2017. **101**: p. 360-380.

40. Bhatt, P. and A. Goe, *Carbon fibres: production, properties and potential use.* Material Science Research India, 2017. **14**(1): p. 52-57.
41. Kandare, E., et al., *Improving the through-thickness thermal and electrical conductivity of carbon fibre/epoxy laminates by exploiting synergy between graphene and silver nano-inclusions.* Composites Part A: Applied Science and Manufacturing, 2015. **69**: p. 72-82.
42. Nakagawa, Y., K.-i. Mori, and T. Maeno, *3D printing of carbon fibre-reinforced plastic parts.* The International Journal of Advanced Manufacturing Technology, 2017. **91**(5): p. 2811-2817.
43. Tekinalp, H.L., et al., *Highly oriented carbon fiber–polymer composites via additive manufacturing.* Composites Science and Technology, 2014. **105**: p. 144-150.
44. Zweben, C.H., *Composites: Overview*, in *Encyclopedia of Condensed Matter Physics*, F. Bassani, G.L. Liedl, and P. Wyder, Editors. 2005, Elsevier: Oxford. p. 192-208.
45. Sun, Z., et al., *Novel application of glass fibers recovered from waste printed circuit boards as sound and thermal insulation material.* Journal of materials engineering and performance, 2013. **22**(10): p. 3140-3146.
46. GuptaV, B. and V. Kothari, *Manufactured fiber technology*. 1997, Chapman and Hall London.
47. Li, X., et al., *Preparation and Mechanical Properties of Fiber Reinforced PLA for 3D Printing Materials.* IOP Conference Series: Materials Science and Engineering, 2018. **322**: p. 022012.
48. Guo, R., et al., *Effect of toughening agents on the properties of poplar wood flour/poly (lactic acid) composites fabricated with fused deposition modeling.* European Polymer Journal, 2018. **107**: p. 34-45.
49. Kruth, J.-P., et al., *Lasers and materials in selective laser sintering.* Assembly Automation, 2003.
50. Contuzzi, N., S. Campanelli, and A. Ludovico, *3D finite element analysis in the selective laser melting process.* International Journal of Simulation Modelling, 2011. **10**(3): p. 113-121.
51. Walczak, R. and K. Adamski, *Inkjet 3D printing of microfluidic structures—on the selection of the printer towards printing your own microfluidic chips.* Journal of micromechanics and microengineering, 2015. **25**(8): p. 085013.
52. Ramakrishnan, T., M. Schlafly, and K.B. Reed. *Evaluation of 3D printed anatomically scalable transfemoral prosthetic knee*. in *2017 International Conference on Rehabilitation Robotics (ICORR)*. 2017. IEEE.
53. Wang, Y., et al., *Current Status and Prospects of Polymer Powder 3D Printing Technologies.* Materials (Basel), 2020. **13**(10).
54. Shi, J., J. Yang, and X. Wang, *Current status and trends in 3D printing technology for multi-material parts.* Mechanical design and Manufacturing engineering, 2017. **46**.
55. Djumas, L., et al., *Enhanced Mechanical Performance of Bio-Inspired Hybrid Structures Utilising Topological Interlocking Geometry.* Scientific Reports, 2016. **6**(1): p. 26706.
56. Zhou, C., et al. *Development of multi-material mask-image-projection-based stereolithography for the fabrication of digital materials*. in *Annual solid freeform fabrication symposium*. 2011.
57. Vaezi, M., et al., *Multiple material additive manufacturing – Part 1: a review.* Virtual and Physical Prototyping, 2013. **8**(1): p. 19-50.
58. Ali, M.H., N. Mir-Nasiri, and W.L. Ko, *Multi-nozzle extrusion system for 3D printer and its control mechanism.* The International Journal of Advanced Manufacturing Technology, 2016. **86**(1): p. 999-1010.

59. Malone, E. and H. Lipson. *Multi-material freeform fabrication of active systems*. in *Engineering Systems Design and Analysis*. 2008.
60. Khalil, S., J. Nam, and W. Sun, *Multi‐nozzle deposition for construction of 3D biopolymer tissue scaffolds.* Rapid Prototyping Journal, 2005.
61. Okwuosa, T.C., et al., *Fabricating a shell-core delayed release tablet using dual FDM 3D printing for patient-centred therapy.* Pharmaceutical research, 2017. **34**(2): p. 427-437.
62. Kim, H., et al., *Experimental Study on Mechanical Properties of Single- and Dual-material 3D Printed Products.* Procedia Manufacturing, 2017. **10**: p. 887-897.
63. Database, P.P., *Stress-strain behavior of polymers*. 2015: PolymerDatabase.com.
64. Geng, Y., et al., *Bio-based polyesters based on 2,5-furandicarboxylic acid as 3D-printing materials: Design, preparation and performances.* European Polymer Journal, 2019. **114**: p. 476-484.
65. Richardson, M. and M. Wisheart, *Review of low-velocity impact properties of composite materials.* Composites Part A: Applied Science and Manufacturing, 1996. **27**(12): p. 1123-1131.
66. Thakur, V.K., *Cellulose-based graft copolymers: structure and chemistry*. 2015: CRC Press.
67. Flores-Johnson, E.A., et al., *Numerical investigation of the impact behaviour of bioinspired nacre-like aluminium composite plates.* Composites Science and Technology, 2014. **96**: p. 13-22.
68. Mirzaeifar, R., et al., *Defect-Tolerant Bioinspired Hierarchical Composites: Simulation and Experiment.* ACS Biomaterials Science & Engineering, 2015. **1**(5): p. 295-304.
69. Zehnder, A.T., *Modes of Fracture*, in *Encyclopedia of Tribology*, Q.J. Wang and Y.-W. Chung, Editors. 2013, Springer US: Boston, MA. p. 2292-2295.
70. Committee., W.T.O.T.B.t.T.T., *Standard Test Methods for Plane-Strain Fracture Toughness and Strain Energy Release Rate of Plastic Materials1*. 2014.
71. Hoeppner, D.W., *Cyclic Loading and Cyclic Stress*, in *Encyclopedia of Tribology*, Q.J. Wang and Y.-W. Chung, Editors. 2013, Springer US: Boston, MA. p. 691-698.
72. Xin, Q., *Durability and reliability in diesel engine system design*, in *Diesel Engine System Design*, Q. Xin, Editor. 2013, Woodhead Publishing. p. 113-202.
73. Kim, W.H. and C. Laird, *Crack nucleation and stage I propagation in high strain fatigue—II. mechanism.* Acta Metallurgica, 1978. **26**(5): p. 789-799.
74. Barthelat, F., *Designing nacre-like materials for simultaneous stiffness, strength and toughness: Optimum materials, composition, microstructure and size.* Journal of the Mechanics and Physics of Solids, 2014. **73**: p. 22-37.
75. Rim, J.E., et al., *Dimensional analysis and parametric studies for designing artificial nacre.* J Mech Behav Biomed Mater, 2011. **4**(2): p. 190-211.
76. Porter, M.M., et al., *3D-printing and mechanics of bio-inspired articulated and multi-material structures.* J Mech Behav Biomed Mater, 2017. **73**: p. 114-126.
77. Byrne, G., et al., *Biologicalisation: Biological transformation in manufacturing.* CIRP Journal of Manufacturing Science and Technology, 2018. **21**: p. 1-32.
78. Wen, R., *Chinese*. Vol. underwater world. 2018, Beijing: People's Education Press.
79. Ding, Y., *Inspiration from marine animals.* Navigation, 1993. **1**.
80. Bechert, D., et al. *Biological surfaces and their technological application-laboratory and flight experiments on drag reduction and separation control*. in *28th Fluid dynamics conference*. 1997.
81. Yang, W., et al., *Natural Flexible Dermal Armor.* Advanced Materials, 2013. **25**(1): p. 31-48.

82. Browning, A., C. Ortiz, and M.C. Boyce, *Mechanics of composite elasmoid fish scale assemblies and their bioinspired analogues.* Journal of the mechanical behavior of biomedical materials, 2013. **19**: p. 75-86.
83. Ghosh, R., H. Ebrahimi, and A. Vaziri, *Frictional effects in biomimetic scales engagement.* EPL (Europhysics Letters), 2016. **113**(3): p. 34003.
84. Vernerey, F.J. and F. Barthelat, *Skin and scales of teleost fish: Simple structure but high performance and multiple functions.* Journal of the Mechanics and Physics of Solids, 2014. **68**: p. 66-76.
85. Yang, W., et al., *The armored carapace of the boxfish.* Acta biomaterialia, 2015. **23**: p. 1-10.
86. Lin, E., et al., *3D printed, bio-inspired prototypes and analytical models for structured suture interfaces with geometrically-tuned deformation and failure behavior.* Journal of the Mechanics and Physics of Solids, 2014. **73**: p. 166-182.
87. Wang, R. and H.S. Gupta, *Deformation and fracture mechanisms of bone and nacre.* Annual Review of Materials Research, 2011. **41**: p. 41-73.
88. Cui, S., Z. Yang, and Z. Lu, *An analytical model for the bio-inspired nacreous composites with interlocked "brick-and-mortar" structures.* Composites Science and Technology, 2020. **193**: p. 108131.
89. Ma, X., H. Liang, and L. Wang, *Multi-materials 3D printing application of shell biomimetic structure.* Chinese Science Bulletin, 2015. **61**(7): p. 728-734.
90. Barthelat, F. and H.D. Espinosa, *An Experimental Investigation of Deformation and Fracture of Nacre–Mother of Pearl.* Experimental Mechanics, 2007. **47**(3): p. 311-324.
91. Cui, F. and Q. Feng, *Biomaterials Science*. 2004: Tsinghua University Press Co., Ltd.
92. Zhang, H. and D. Li, *Determination of interfacial bonding strength using a cantilever bending method with in situ monitoring acoustic emission.* Surface and Coatings Technology, 2002. **155**(2-3): p. 190-194.
93. Deng, Z., *Study of the laminar structure of clam shells and their properties*. 2011, University of Jilin.
94. Espinosa, H.D., et al., *Tablet-level origin of toughening in abalone shells and translation to synthetic composite materials.* Nature Communications, 2011. **2**(1): p. 173.
95. Ghimire, A., et al., *Tunable interface hardening: Designing tough bio-inspired composites through 3D printing, testing, and computational validation.* Composites Part B: Engineering, 2021. **215**: p. 108754.
96. Khandelwal, A., et al., *Crack propagation in staggered structures of biological and biomimetic composites.* Computational Materials Science, 2017. **126**: p. 238-243.
97. Ji, B. and H. Gao, *Mechanical properties of nanostructure of biological materials.* Journal of the Mechanics and Physics of Solids, 2004. **52**(9): p. 1963-1990.
98. Baughman, R.H., et al., *Negative Poisson's ratios as a common feature of cubic metals.* Nature, 1998. **392**(6674): p. 362-365.
99. Lakes, R.S., *Negative-Poisson's-Ratio Materials: Auxetic Solids.* Annual Review of Materials Research, 2017. **47**(1): p. 63-81.
100. Lakes, R., *A broader view of membranes.* Nature, 2001. **414**(6863): p. 503-504.
101. Babaee, S., et al., *3D soft metamaterials with negative Poisson's ratio.* Adv Mater, 2013. **25**(36): p. 5044-9.
102. works, N., *Datasheet of Ingeo biopolymer*, in *PLA*, Makergear. 2015.

103. Esun Induustrial Co, L. *3D printing photopolymer resincseries*. Available from: http://www.esun3d.net/products/361.html.
104. *Elastollan® TPU technical data sheet*, B.c. company.
105. Simplify3D, C.L. *Print quality troubleshooting guide*. 2015; Available from: https://www.simplify3d.com/support/print-quality-troubleshooting/.
106. Roylance, D., *Introduction to fracture mechanics.* 2001.
107. Ko, K., et al., *Bio-inspired bimaterial composites patterned using three-dimensional printing.* Composites Part B: Engineering, 2019. **165**: p. 594-603.
108. Rabiei, R., S. Bekah, and F. Barthelat, *Failure mode transition in nacre and bone-like materials.* Acta Biomaterialia, 2010. **6**(10): p. 4081-4089.
109. Smith, B.L., et al., *Molecular mechanistic origin of the toughness of natural adhesives, fibres and composites.* Nature, 1999. **399**(6738): p. 761-763.
110. Dimas, L.S., et al., *Tough Composites Inspired by Mineralized Natural Materials: Computation, 3D printing, and Testing.* Advanced Functional Materials, 2013. **23**(36): p. 4629-4638.
111. Lemaitre, J., *A course on damage mechanics*. 2012: Springer Science & Business Media.
112. Moetazedian, A., et al., *Damage in extrusion additive manufactured biomedical polymer: Effects of testing direction and environment during cyclic loading.* Journal of the Mechanical Behavior of Biomedical Materials, 2021. **118**: p. 104397.

Appendix

Table 6.1. Energy dissipation of multi-material structures for each cycle under cyclic tensile test.

			Modulus	Damage resistance (mJ/mm^3)
0degree	unloading	first loading repetition	15.004	
	cycle 1	last unloading repetition	15.852	-0.057
	cycle 2	last unloading repetition	13.995	0.067
5degree	unloading	first loading repetition	12.906	
	cycle 1	last unloading repetition	13.250	-0.027
	cycle 2	last unloading repetition	11.620	0.100
	cycle 3	last unloading repetition	10.194	0.210
	cycle 4	last unloading repetition	0.596	0.954
	cycle 5	last unloading repetition	0.301	0.977

Table 6.2. Tensile results for all specimens.

		UTS (MPa)	Max force(N)	Modulus (MPa)	Area before UTS (mJ/mm^3)	Total area (mJ/mm^3)
PLA&TPU-0degree	sample 1	5.93	209.58	491.60	5.75	65.83
	sample 2	6.06	221.68	403.65	5.62	67.56
	sample 5	5.96	160.40	395.45	4.22	56.92
	sample 4	4.45	159.86	394.95	4.09	58.64
	Average	5.60	187.88	443.28	4.92	62.24
	Standard deviation	0.77	32.76	68.35	1.17	5.09
PLA&TPU-1degree	sample 1	9.96	323.66	450.25	14.28	80.39
	sample 2	9.69	317.83	348.36	17.57	86.69
	sample 4	8.85	294.43	515.06	9.72	78.98
	sample 5	10.76	362.94	499.86	14.64	90.35
	Average	9.98	327.40	453.38	14.35	85.77
	Standard deviation	0.79	28.44	75.28	3.24	5.35
PLA&TPU-3degree	sample 1	7.01	227.55	460.44	10.13	96.46
	sample 2	12.43	433.95	398.78	28.74	107.43
	sample 3	10.56	354.01	526.29	16.47	81.90
	sample 4	9.68	322.27	444.05	17.49	80.41
	new nozzle	13.16	397.00	473.96	24.60	99.76
	Average	10.57	346.96	347.49	18.20	91.55
	Standard deviation	2.43	79.04	234.55	7.74	12.82
PLA&TPU-5degree	sample 1	11.56	378.26	458.43	22.08	87.69
	sample 2	10.73	351.41	492.51	17.59	93.24
	sample 3	12.19	408.83	536.96	21.67	73.82
	sample 4	10.25	342.54	486.85	23.09	89.72
	new nozzle	12.58	389.94	555.97	22.96	76.32
	Average	11.46	374.19	495.96	20.45	84.92
	Standard deviation	0.97	27.32	39.38	2.49	10.00
PLA&TPU-9degree	sample 1	6.02	194.92	218.03	11.86	108.64
	sample 2	7.48	244.82	398.26	11.32	74.98
	sample 3	6.35	20.09	274.31	11.29	87.86
	sample 5	5.35	168.84	324.46	11.45	76.98
	sample 6	5.36	183.65	267.24	10.43	82.73
	sample 7	5.69	196.97	446.63	9.72	85.74
	new nozzle 1	6.91	191.07	519.80	7.40	82.15
	new nozzle 2	8.94	261.72	567.02	11.06	78.68
	Average	6.51	182.76	395.48	10.58	86.46
	Standard deviation	1.23	72.86	150.88	1.81	13.28
Pure PLA	sample 1	51.74	1345.53	2646.06	60.97	51.66
	sample 2	42.57	1263.69	2777.36	52.40	47.54
	Average	47.16	1304.61	2711.71	56.68	49.60
	Standard deviation	6.49	57.87	92.84	6.06	2.91
PLA&PLA-0degree	sample 1	23.37	775.09	2538.23	11.51	13.70
	sample 2	32.51	1061.62	2667.97	32.32	38.66
	Average	27.94	918.35	2603.10	21.91	26.18
	Standard deviation	6.46	202.61	91.74	14.72	17.66
PLA&PLA-5degree	sample 1	24.46	783.01	2811.72	13.29	13.66
	sample 2	31.01	954.59	2613.13	21.52	23.67
	Average	27.73	868.80	2712.42	17.40	18.66
	Standard deviation	4.63	121.33	140.42	5.82	7.08